

Supporting Information

Synergistic global and local flexibilities in Zr-based metal-organic frameworks enable sequential sieving of hexane isomers

*Rundao Chen, †^a Jiaqi Li, †^a Fang Zheng, *^b Fangru Zhou,^a Bin Sheng,^a Baojian Liu,^b Qiwei Yang,^{a,b} Zhiguo Zhang,^{a,b} Qilong Ren,^{a,b} and Zongbi Bao*^{a,b}*

^a Key Laboratory of Biomass Chemical Engineering of the Ministry of Education, College of Chemical and Biological Engineering, Zhejiang University, 866 Yuhangtang Road, Hangzhou 310058. E-mail: baozb@zju.edu.cn

^b Institute of Zhejiang University-Quzhou, Zhejiang University, 99 Zheda Road, Quzhou 324000. E-mail: zhengfang_@zju.edu.cn

This Supporting Information includes:

Experimental Methods

Figure S1 to S64

Table S1 to S10

References

Table of Contents

Experimental Methods	3
Figure S1-S3. Rietveld refinements	8
Figure S4-S6. N ₂ adsorption-desorption isotherms.....	11
Figure S7. Thermogravimetric curves.....	14
Figure S8-S22. Hexane isomer vapor adsorption isotherms	15
Figure S23. Isosteric heats of adsorption of hexane isomers	30
Figure S24-S26. Gravimetric adsorption and DSC measurements	31
Figure S27-S29. Hexane isomer diffusion kinetics.....	34
Figure S30. Mass-transfer coefficients fitting curves	37
Figure S31-S40. Binary equimolar breakthrough curves.....	38
Figure S41. Summary of breakthrough selectivities	48
Figure S42-S57. Quinary equimolar breakthrough curves.....	49
Figure S58. Liquid-phase adsorption	65
Figure S59-S61. Stability tests	66
Figure S62-S64. In-situ PXRD curves and DRIFTS spectra	69
Table S1. Physical properties of hexane isomers	72
Table S2-S5. Rietveld refinement results	73
Table S6. Adsorption capacity of hexane isomers on various materials.....	77
Table S7. Heats of adsorption of hexane isomers	79
Table S8. LDF mass-transfer coefficients of n-Hex.....	80
Table S9. Surface area and pore volume	81
Table S10. DFT calculation results	82
References	83

Experimental Methods

Materials and physical measurements: All chemicals (AR grade) were used as received from commercial suppliers without further purification. Zirconium chloride (ZrCl_4 , 99.9%), hafnium chloride (HfCl_4 , 98%), fumaric acid (fum, 99%), mesaconic acid (mes, 99%), formic acid (FA, 96%), methanol (MeOH, 99.9%), and potassium hydroxide (KOH, AR) were purchased from Sigma-Aldrich. Hexane isomers including n-hexane (n-Hex, 96%), 2-methylpentane (2-MP, 98%), 3-methylpentane (3-MP, 99%), 2,3-dimethylbutane (2,3-DMB, 98%), 2,2-dimethylbutane (2,2-DMB, 98%), and n-heptane (99%) were purchased from TCI. Ultrahigh-purity helium (>99.999%) and nitrogen (>99.999%) were supplied by Jingong Industrial. Thermogravimetric (TG) analysis was performed on a TA Discovery SDT 650 simultaneous thermal analyzer with a heating rate of 10 K/min under N_2 environment from 323 to 1073 K. Adsorption-desorption isotherms of N_2 at 77 K were measured on a Micromeritics 3Flex gas adsorption analyzer. The initial outgassing process was carried out under high vacuum at 373 K for 24 h before adsorption measurements and about 100 mg of the activated sample was used for gas adsorption studies. The free space of the system was determined using helium gas.

Synthesis of Zr-fum-FA, Hf-fum-FA, and Zr-mes-FA: Fumaric acid (116 mg, 1 mmol) was added to a solution of ZrCl_4 (466 mg, 2 mmol) in formic acid (5 mL) and deionized water (250 μL) in a 20 mL Teflon-lined reactor. After ultrasonication for 10 minutes, the reaction was heated in an oven at 393 K for 72 hours. When the reaction was cooled to room temperature, the white powder product of Zr-fum-FA was collected by filtration, washed with water and MeOH, the trapped solvents were further exchanged with MeOH for 6 times (8 hours per time), and the sample was activated under high vacuum at 373 K for 24 h before measurements.

The synthesis method of Hf-fum-FA was similar to that of Zr-fum-FA, except that ZrCl_4 (466 mg, 2 mmol) was replaced by HfCl_4 (641 mg, 2 mmol), yielding Hf-fum-FA as a white fine powder.

For the synthesis of Zr-mes-FA, mesaconic acid (260 mg, 2 mmol) was added to a solution of ZrCl_4 (233 mg, 1 mmol) in formic acid (5 mL) and deionized water (250 μL) in a 20 mL Teflon-lined reactor, followed by the same treatment of Zr-fum-FA and Hf-fum-FA.

Powder X-ray diffraction analysis and Rietveld refinements: Powder X-ray diffraction (PXRD) analysis of finely ground MOF samples was carried out on a Rigaku SmartLab SE diffractometer equipped with a $\text{Cu K}\alpha$ emission radiation ($\lambda = 1.5406 \text{ \AA}$, 40 kV, 50 mA) and D/teX Ultra 250 1D detector. The data were collected at room temperature in a range of $3\text{-}130^\circ$ (2θ) with a scan speed of $2^\circ/\text{min}$ ($0.01^\circ/\text{step}$) and an incident slit of $1/4$ degree. The sample stage was rotated along the beta axis with a spin speed of 120 rpm to better offset the impact of

the preferred orientation. The initial structure of Zr-fum-FA, Zr-mes-FA, and Hf-fum-FA were modified from the similar structure of MIP-203-F¹(CCDC 1964389), and refined by Rietveld methods using the Rigaku SmartLab Studio II software suit.

Single-component vapor adsorption measurements: Single-component isotherms of n-Hex, 2-MP, 3-MP, 2,3-DMB, and 2,2-DMB were collected up to 20 kPa at 303, 333, 363, 393 and 423 K on a MicrotracMRB BELSORP-max II vapor adsorption analyzer. The initial outgassing process was carried out under high vacuum at 373 K for 24 h before adsorption measurements and about 50 mg of the activated sample was used for adsorption tests.

The heats of adsorption were determined by the variant form of the Clausius-Clapeyron equation:

$$Q_{st} = \frac{RT_1T_2}{T_2 - T_1} (\ln P_2 - \ln P_1)$$

where Q_{st} is the isosteric heat of adsorption, R is the gas constant, P_1 and P_2 are the equilibrium pressures of a given adsorption amount at testing temperatures T_1 and T_2 , respectively, which are determined by the interpolation of hexane isotherms at 303 and 423 K using the BEL Master software.

The DSC-derived heats of adsorption were calculated by the equation:

$$Q_{ads} = \frac{\int_0^{t_e} P dt}{q_e}$$

where Q_{ads} is the heat of adsorption, t_e is the time to reach adsorption equilibrium, P is the normalized heat flow of the system (W/g, baseline subtracted), and q_e is the equilibrium adsorption amount (mmol/g).

Adsorption kinetics: The vapor kinetic adsorption characteristics were measured concurrently with the single-component adsorption experiments. The kinetic profile corresponding to the first point on the isotherm was used for mass-transfer coefficient fitting. With a dosing amount of 0.5 cm³/g, changes of pressures of the sample tube and manifold system were recorded over time (t , s) before and after vapor dosing until equilibrium was reached. These time-dependent changes were converted into transient adsorption amounts as functions of time. The mass-transfer coefficient (K , s⁻¹) was fitted using the classical linear driving force (LDF) model², and the activation energy of diffusion (E_a) is calculated using the Arrhenius equation:

$$\ln K = -\frac{E_a}{RT} + \ln A$$

where E_a is the activation energy of diffusion, R is the gas constant, K is the mass-transfer coefficient, T is the temperature, and A is a constant.

Gravimetric and differential scanning calorimetry measurements: Enthalpy of adsorption for n-Hex, 2-MP, 3-MP, 2,3-DMB, and 2,2-DMB on Zr-fum-FA were measured using a TA Discovery SDT 650 simultaneous thermal analyzer. In a typical experiment, about 10 mg of activated Zr-fum-FA powder sample was packed into an alumina pan. The baseline was obtained firstly under N₂ flow at the rate of 50 mL/min at 303 K, then the N₂ flow was bubbled through bubblers loaded with 25 mL of single-component n-Hex, 2-MP, 3-MP, 2,3-DMB, and 2,2-DMB placed in water bath for temperature control (291.6, 283.8, 286.3, 281.1, and 273.7 K for n-Hex, 2-MP, 3-MP, 2,3-DMB, and 2,2-DMB respectively to control the vapor pressures to be 15 kPa), then the gas was introduced into the sample chamber at 303 K. TG and DSC signals were collected synchronously for hours to obtain uptake and heat of adsorption respectively. The DSC measurements were conducted thrice for each adsorbate.

Column breakthrough experiments: In a glovebox filled with N₂, 500, 570, and 710 mg of the activated Zr-fum-FA, Zr-mes-FA, and Hf-fum-FA samples were packed into stainless-steel columns (4.6 mm i.d. × 50 mm), respectively. N₂ flow (20 mL/min at 373 K) was introduced into the column to further purge the samples before the breakthrough measurements. N₂ flow at a set rate of 1.0 mL/min was bubbled through a mixture of hexane isomers according to the following volumes (the volumes were determined through trial and error and calculated by GC: the experiment was run without any sample and the vapor phase ratios were optimized to an equimolar mixture): 6.8 mL of n-Hex, 5.3 mL of 3-MP, 4.8 mL of 2-MP, 4.2 mL of 2,3-DMB, and 3.1 mL of 2,2-DMB were in a bubbler placed in a water bath for temperature control (290 K) and mixed gas was introduced into the column at 303 K. The outlet gas from the column was monitored using a SHIMADZU GC-2010 Plus gas chromatograph equipped with an HP-PONA column (50 m × 0.25 mm I.D., 0.5 μm) and flame ionization detector (FID). The temperature settings for the injection port, column, and detector were 150, 50, and 180°C, respectively, with a carrier gas (N₂) flow rate of 0.3 mL/min. After every breakthrough measurement, the columns were regenerated with a N₂ flow of 20 mL/min at 373 K for 24 h to be ready for the next breakthrough test.

The adsorption capacity for each vapor component (q_i , mmol/g) was calculated using the equation:

$$q_i = \frac{(Ft - V_{dead})C_{0,i} - \int_0^t FC_{e,i}\Delta t}{m}$$

where F (mL/min) represents the total flow rate, t (min) is the adsorption time, V_{dead} (mL) is the dead volume of the system (determined using helium), $C_{0,i}$ (mmol/mL) is the inlet concentration

of component i , $C_{e,i}$ (mmol/mL) is the effluent concentration of component i , and m (g) is the mass of the adsorbents.

The dynamic adsorption selectivity (S) for component i relative to component j was then calculated according to the equation:

$$S = \frac{q_i/x_i}{q_j/x_j}$$

where x_i is the molar fraction of the component i in the inlet stream.

Liquid-phase adsorption experiments: Approximately 50 mg of activated MOF samples were immersed in 3 mL of equimolar liquid mixture of *n*-Hex, 3-MP, and 2,2-DMB at temperatures of 303 K and 393 K for 6 h. Subsequently, the adsorbents were collected through filtration, followed by the addition of 1 mL of saturated aqueous solution of KOH to decompose the sample, and 0.5 mL of *n*-heptane to extract the hexane isomers. The organic phase was then collected and analyzed using gas chromatography.

Recyclability tests: To ascertain the reusability of MOF samples in the adsorption of *n*-Hex, a series of adsorption-desorption cycles were conducted using a TA Discovery SDT 650 simultaneous thermal analyzer. In these tests, a sample of approximately 10 mg of activated Zr-fum-FA was placed in the sample chamber under a nitrogen atmosphere at 363 K. A *n*-Hex-balanced N₂ flow (10 mL/min, $p_{n\text{-Hex}} = 10$ kPa) was introduced to facilitate the adsorption process. The mass uptake was monitored for 30 min to reach the adsorption equilibrium. Subsequently, the pure N₂ flow of 100 mL/min was introduced into the chamber for reactivation, and the temperature was elevated to 403 K with a heating rate of 10 K/min and maintained for 30 min to ensure complete desorption. The system was then returned to 363 K before commencing the next cycle.

In-situ powder X-ray diffraction measurements: In-situ PXRD experiments were conducted on a Rigaku SmartLab diffractometer equipped with a high-intensity rotating anode Cu K α radiation source (45 kV, 200 mA) and a ReactorX in-situ sample chamber. The scans were carried out on activated samples under a pure N₂ flow (50 mL/min) or on pre-saturated samples under a 3-MP-balanced N₂ flow (50 mL/min, $p_{3\text{-MP}} = 1$ kPa) from 303 to 423 K, with a controlled heating rate of 5 K/min. Diffraction data were collected within a 2θ range of 5 to 25°.

Variable-temperature diffuse reflectance infrared Fourier transform spectroscopy: VT-DRIFTS experiments were conducted on a Nicolet iS50 FTIR spectrometer with diffuse reflectance optics and a Harrick in-situ sample chamber. The samples in the chamber were reactivated under N₂ flow (50 mL/min) at 373 K for 2 h, followed by collecting baseline at

room temperature. The VT-FTIR spectra were then obtained at 303, 333, 363, 393, and 423 K respectively, with a heating rate of 5 K/min, and a holding time of 10 min before each measurement.

DFT calculations: First-principles density functional theory (DFT) calculations were performed using the CASTEP code³. All calculations were conducted under the generalized gradient approximation with the Perdew-Burke-Ernzerhof function (GGA-PBE)⁴. A semiempirical addition of dispersive forces was included in the calculation to account for van der Waals interactions⁵. A cutoff energy of 544 eV and $1 \times 1 \times 1$ k-point mesh were found to be enough for the total energy to cover within 2×10^{-6} eV/atom. Hexane molecules were introduced to different locations along the diffusion pathways in the one-dimensional pores of Zr-fum-FA or artificially constructed structures to calculate the relative diffusion activation energies.

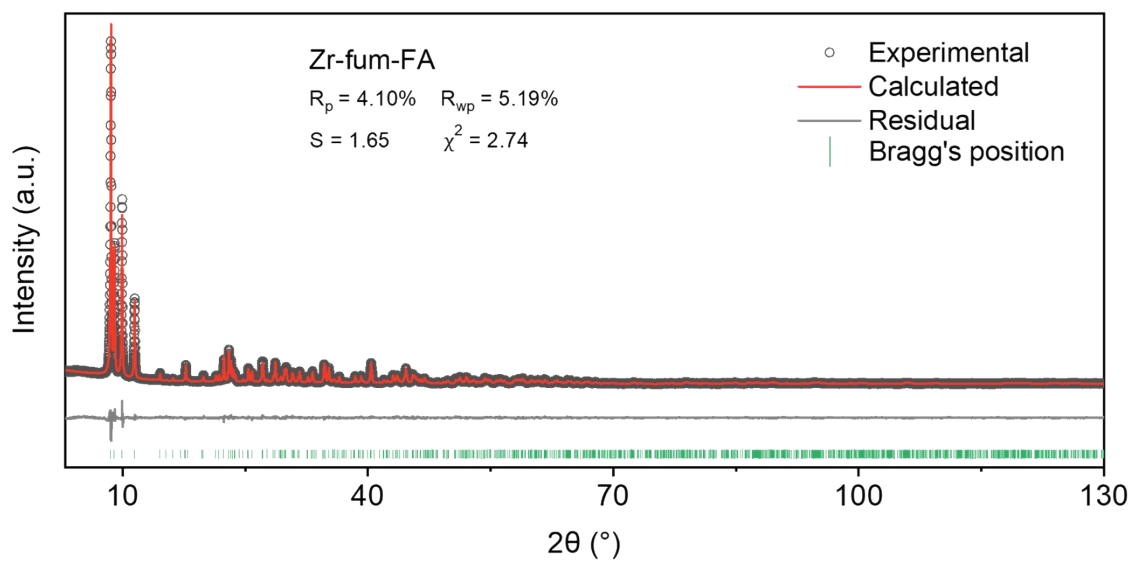


Figure S1. Rietveld refinement of PXRD data for Zr-fum-FA.

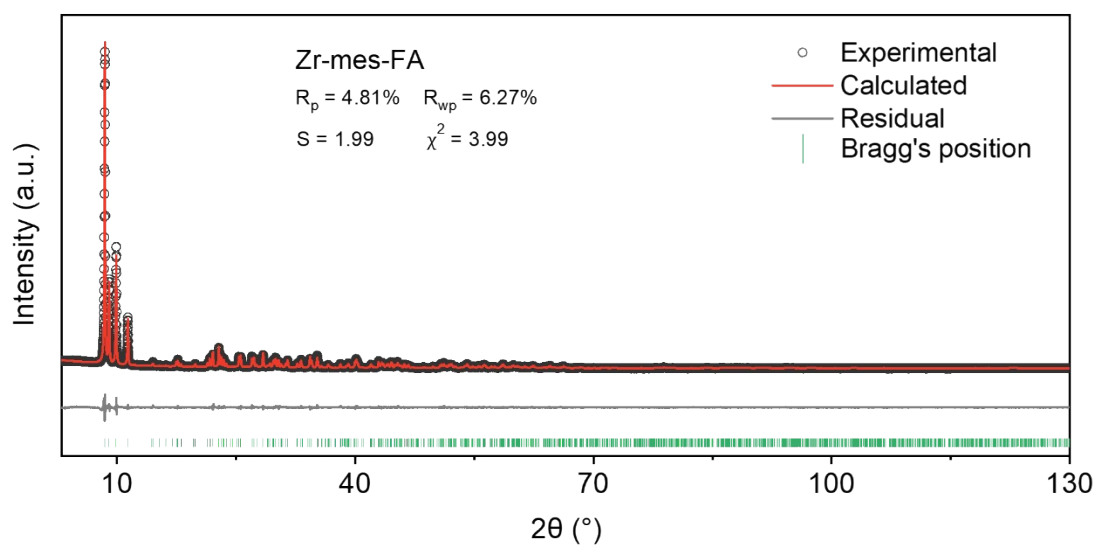


Figure S2. Rietveld refinement of PXRD data for Zr-mes-FA.

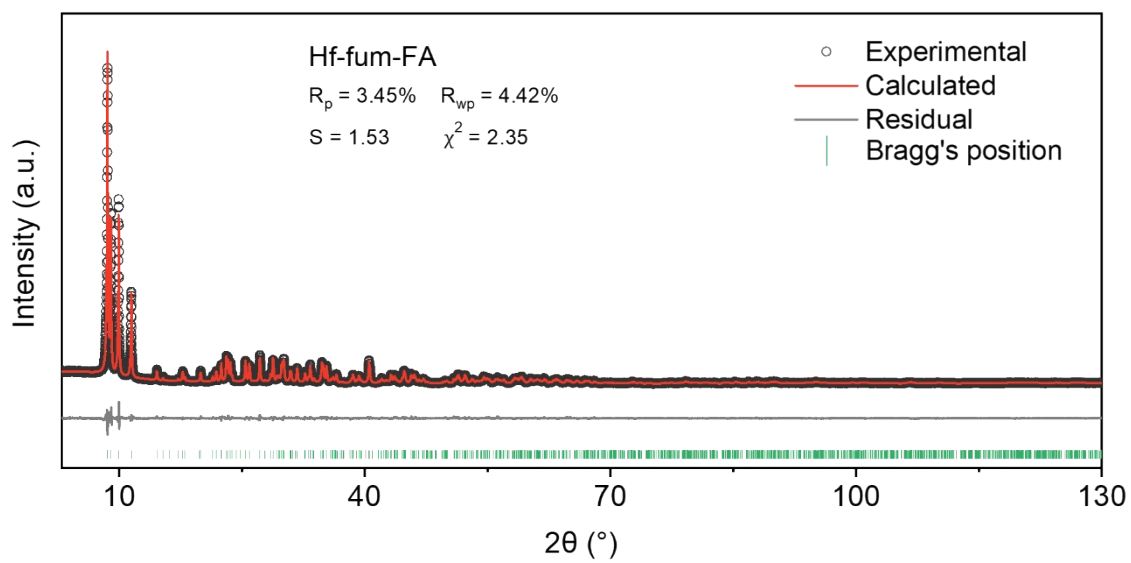


Figure S3. Rietveld refinement of PXRD data for Hf-fum-FA.

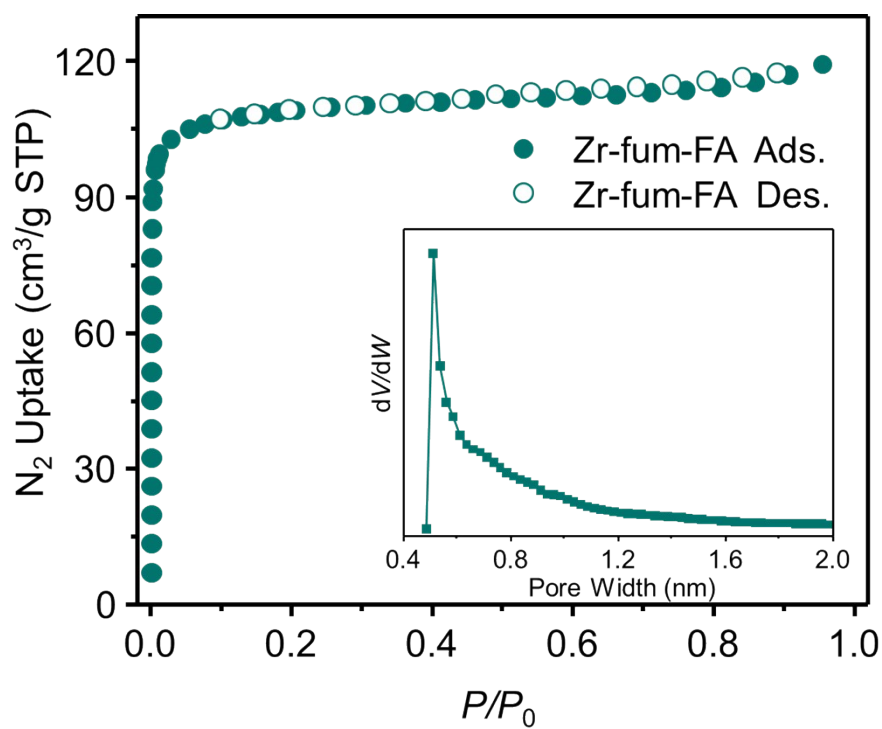


Figure S4. N₂ adsorption-desorption isotherms on Zr-fum-FA at 77 K. Insert: Horvath-Kawazoe pore size distribution.

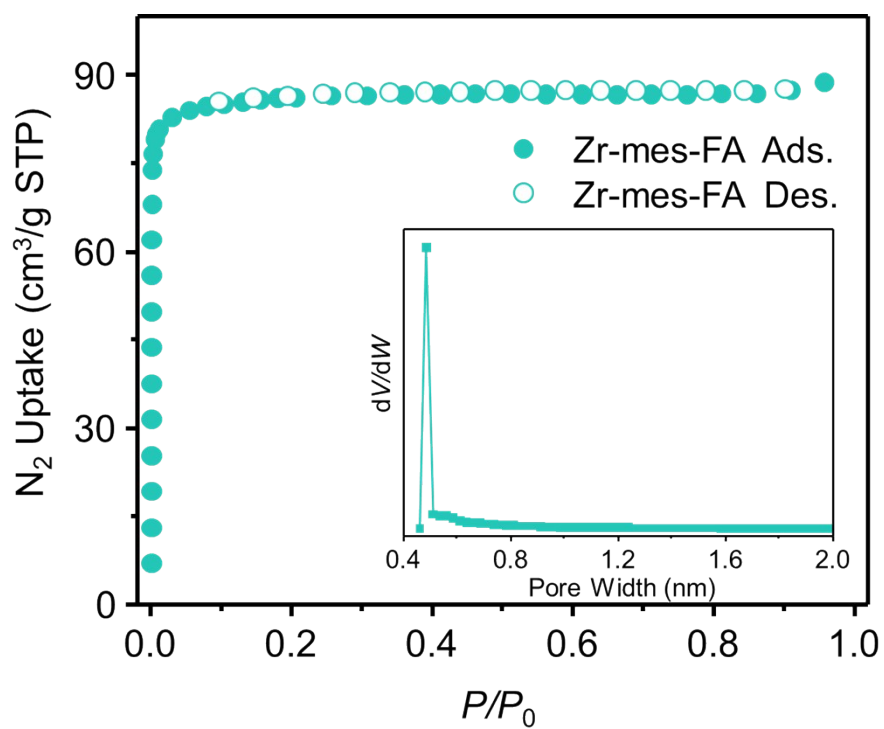


Figure S5. N₂ adsorption-desorption isotherms on Zr-mes-FA at 77 K. Insert: Horvath-Kawazoe pore size distribution.

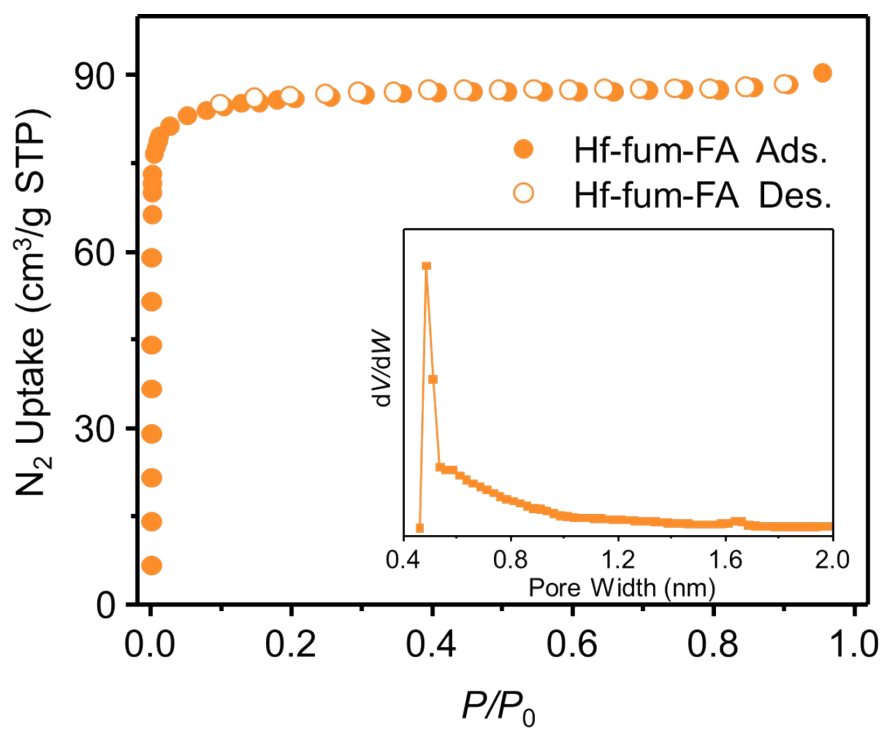


Figure S6. N₂ adsorption-desorption isotherms on Hf-fum-FA at 77 K. Insert: Horvath-Kawazoe pore size distribution.

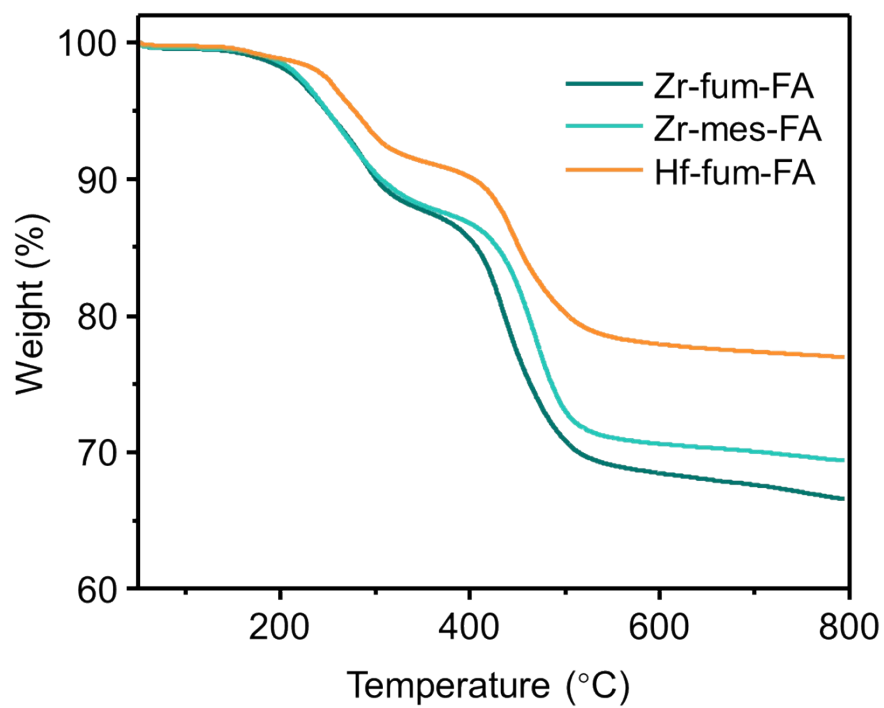


Figure S7. TG curves of activated Zr-fum-FA, Zr-mes-FA, and Hf-fum-FA powder samples under N₂ atmosphere.

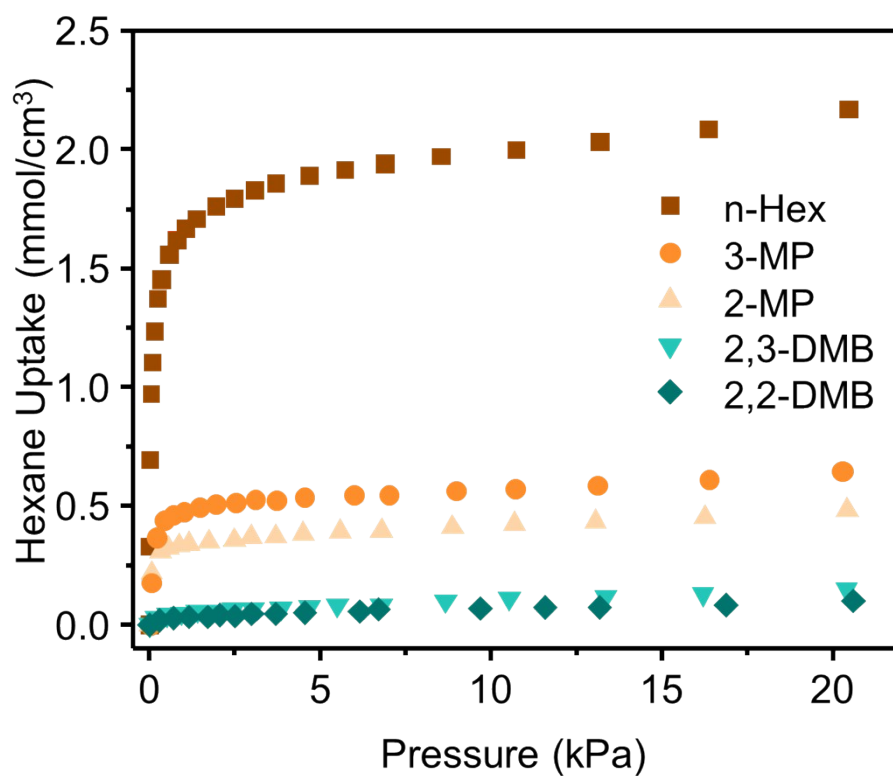


Figure S8. Single-component hexane isomer vapor isotherms on Zr-fum-FA up to 20 kPa at 303 K.

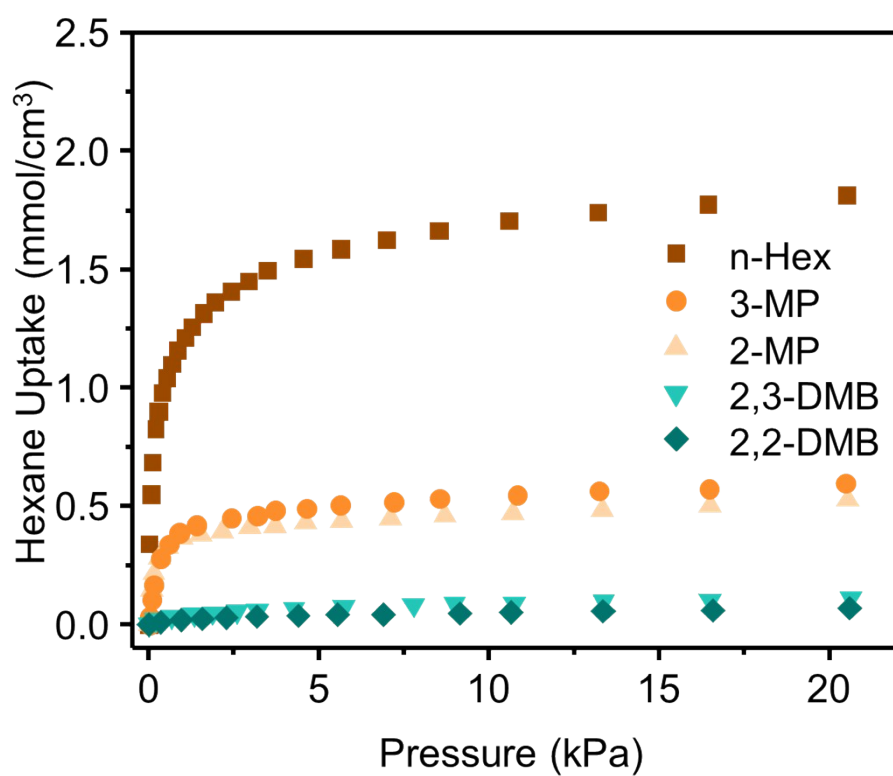


Figure S9. Single-component hexane isomer vapor isotherms on Zr-fum-FA up to 20 kPa at 333 K.

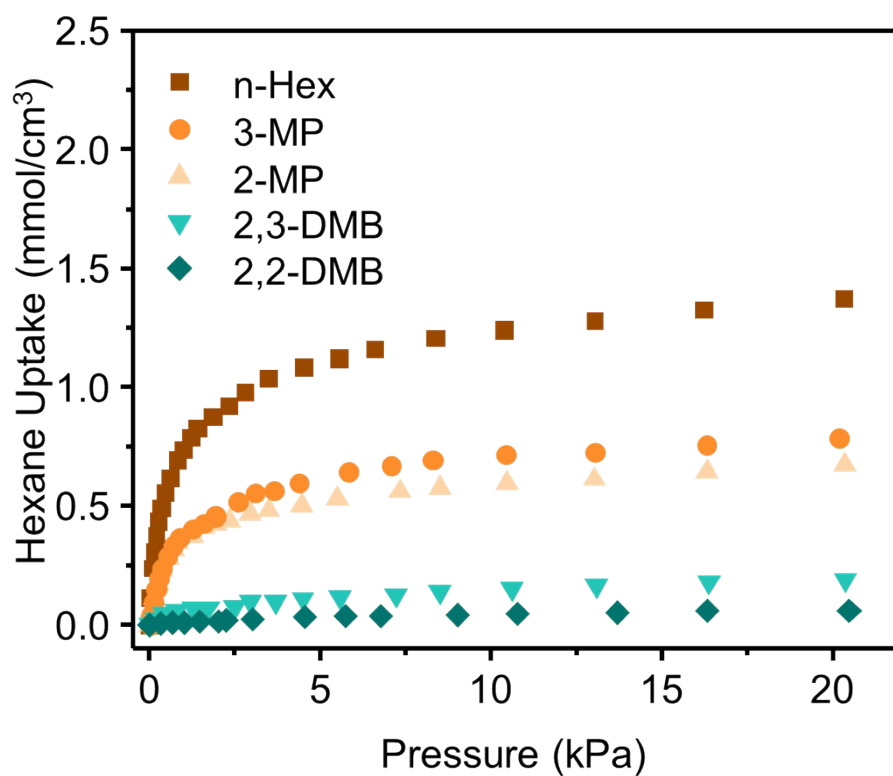


Figure S10. Single-component hexane isomer vapor isotherms on Zr-fum-FA up to 20 kPa at 363 K.

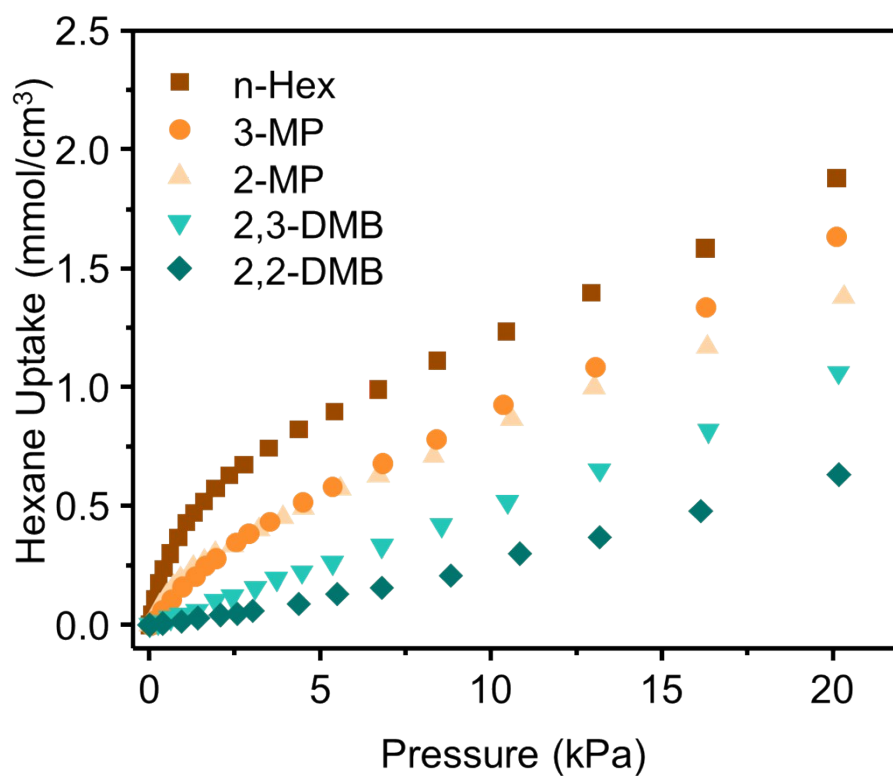


Figure S11. Single-component hexane isomer vapor isotherms on Zr-fum-FA up to 20 kPa at 393 K.

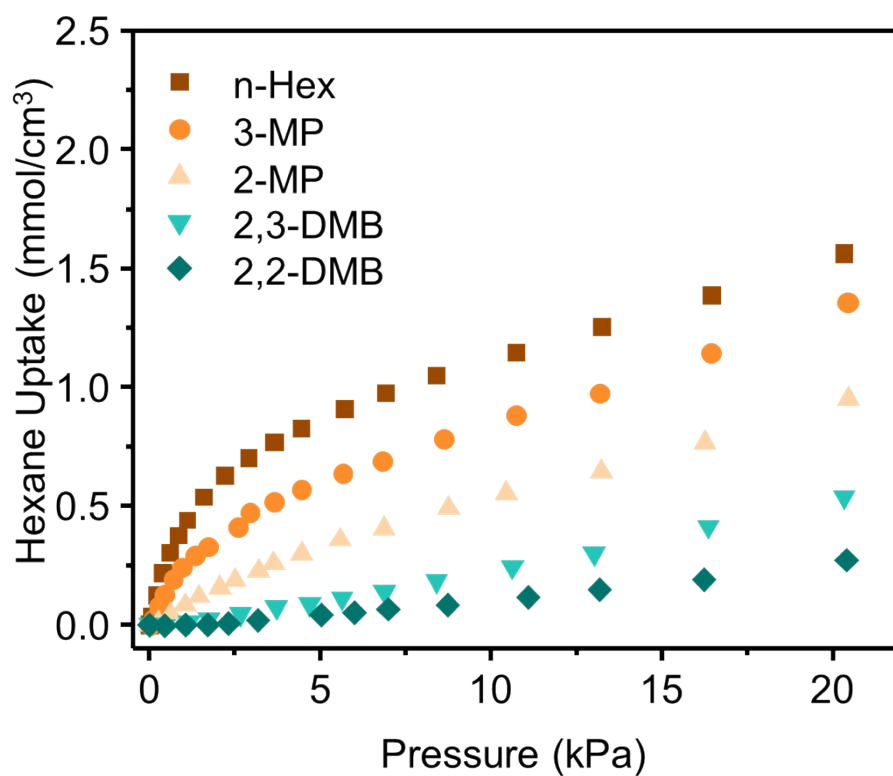


Figure S12. Single-component hexane isomer vapor isotherms on Zr-fum-FA up to 20 kPa at 423 K.

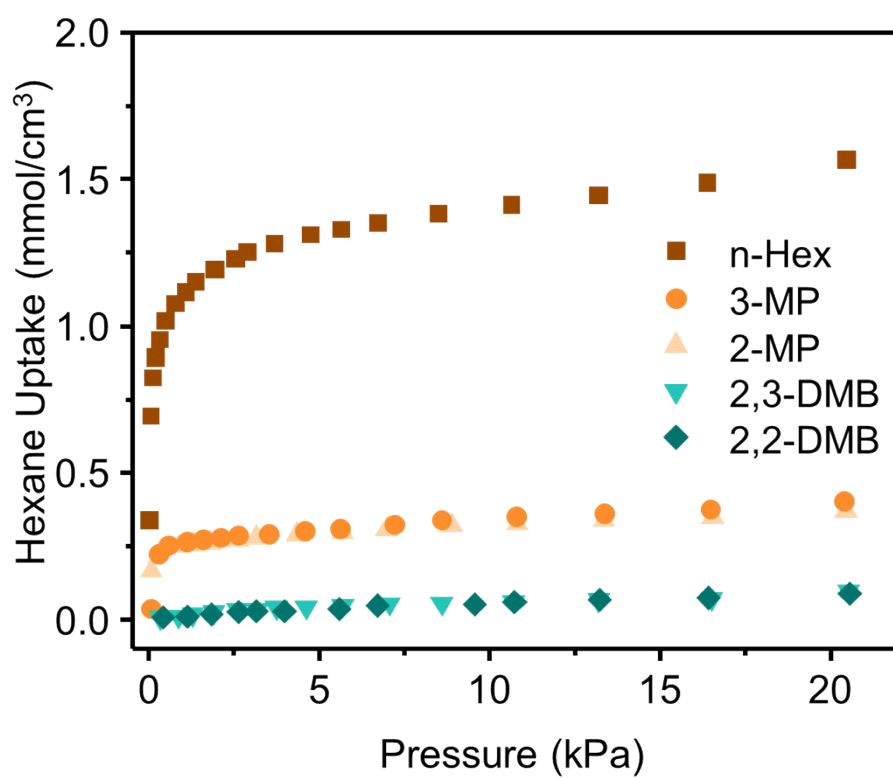


Figure S13. Single-component hexane isomer vapor isotherms on Zr-mes-FA up to 20 kPa at 303 K.

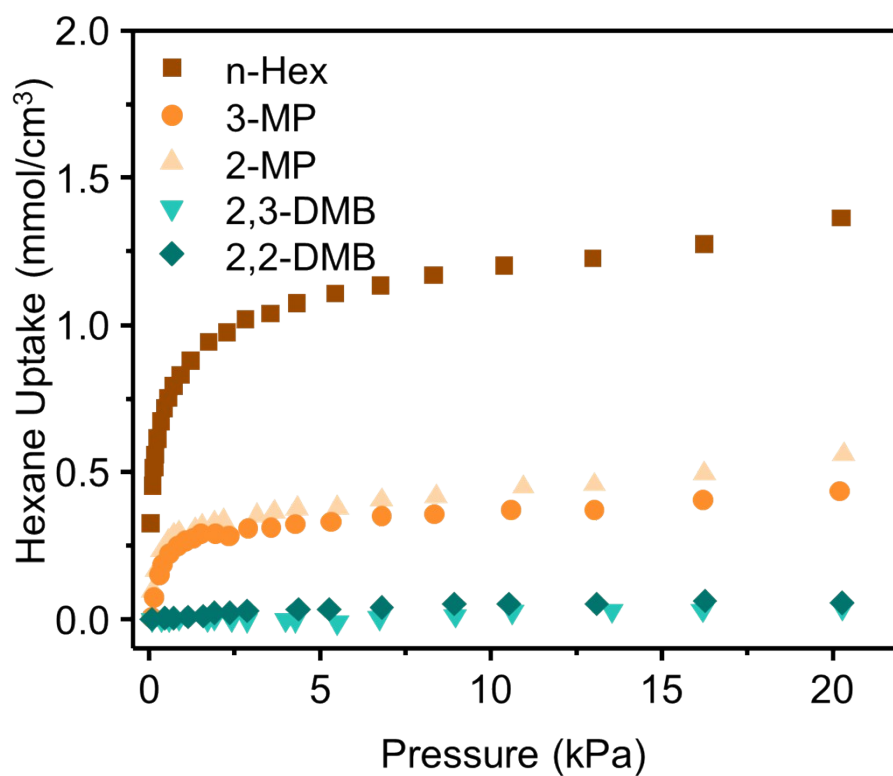


Figure S14. Single-component hexane isomer vapor isotherms on Zr-mes-FA up to 20 kPa at 333 K.

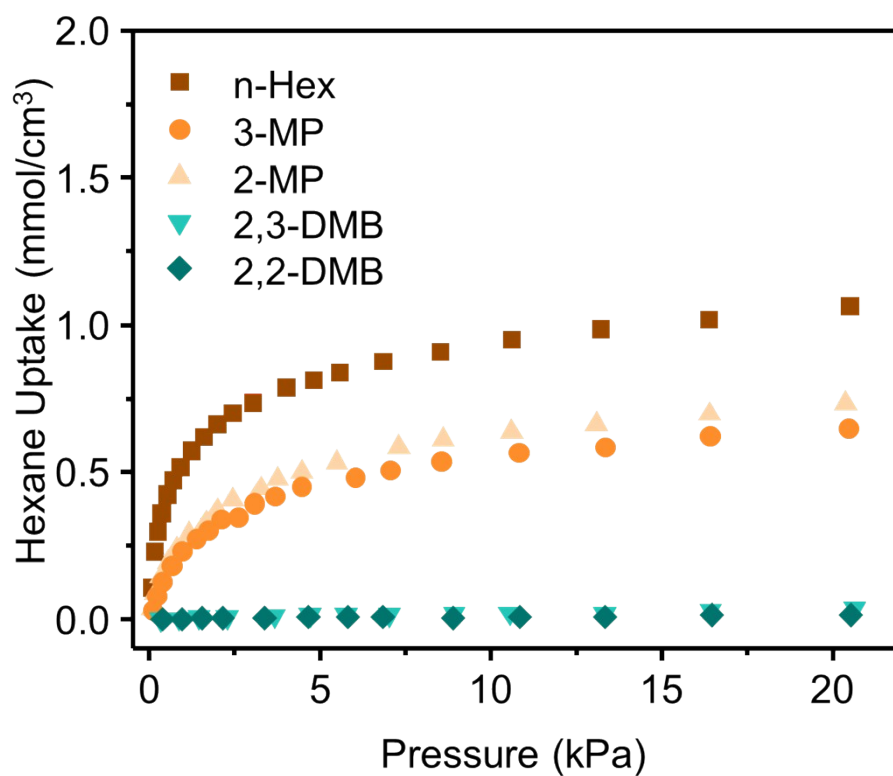


Figure S15. Single-component hexane isomer vapor isotherms on Zr-mes-FA up to 20 kPa at 363 K.

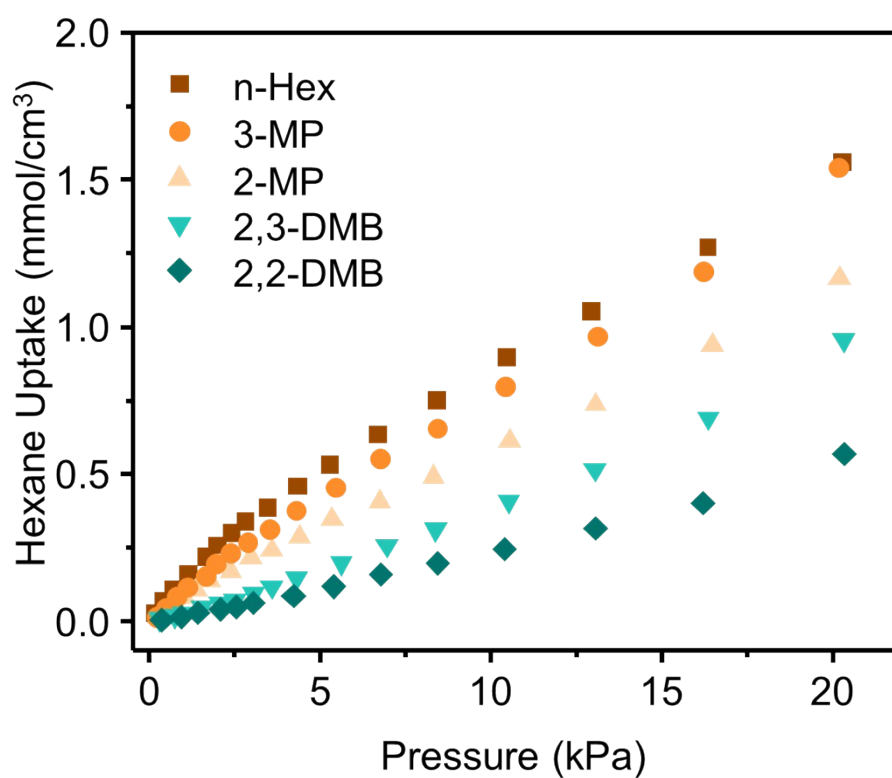


Figure S16. Single-component hexane isomer vapor isotherms on Zr-mes-FA up to 20 kPa at 393 K.

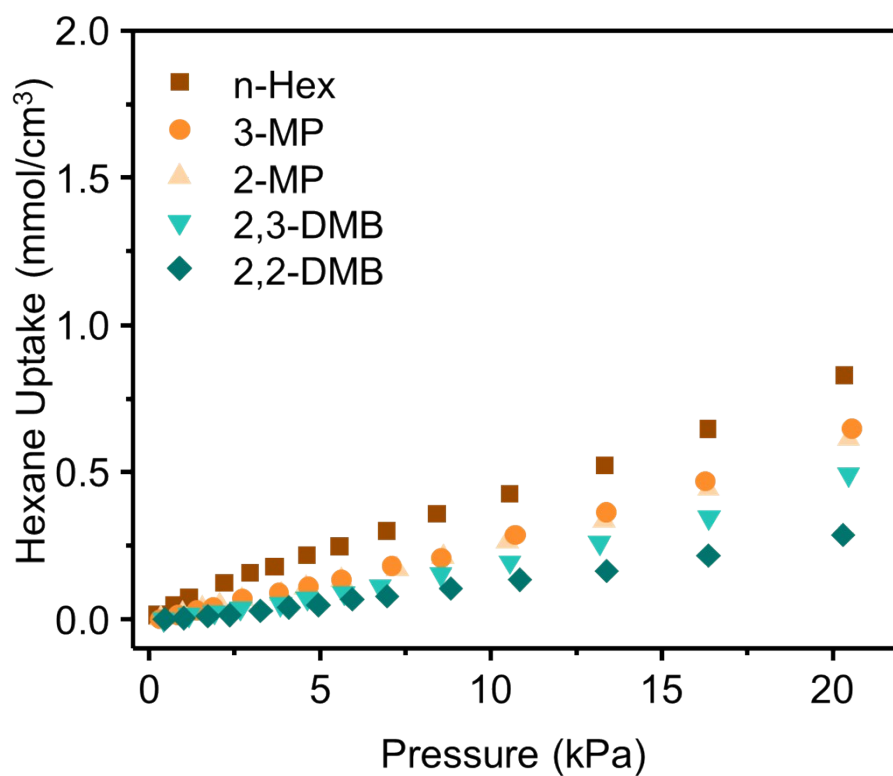


Figure S17. Single-component hexane isomer vapor isotherms on Zr-mes-FA up to 20 kPa at 423 K.

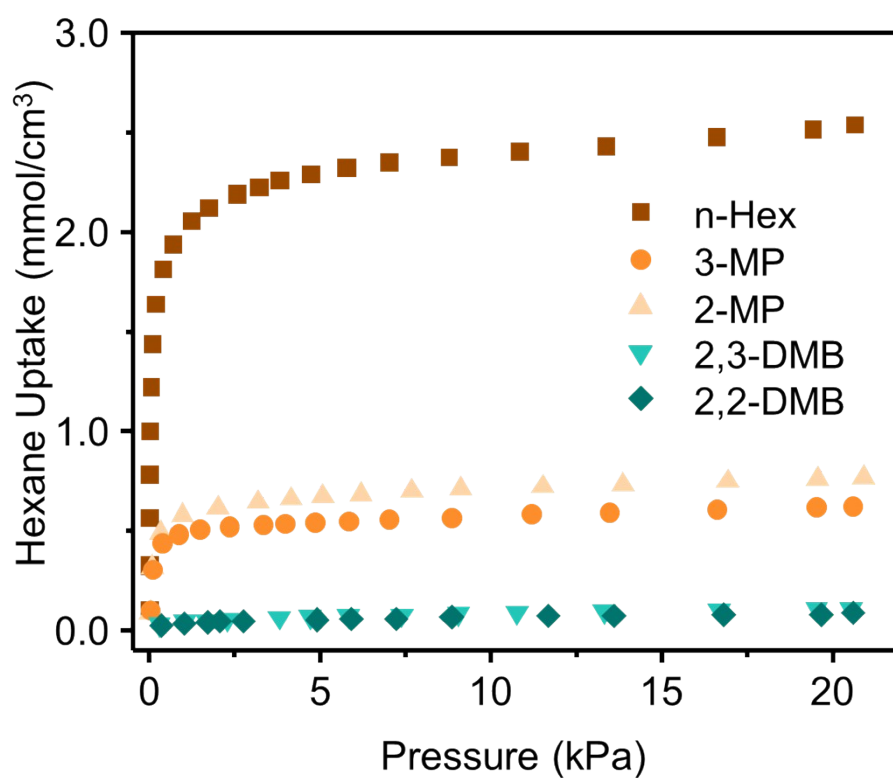


Figure S18. Single-component hexane isomer vapor isotherms on Hf-fum-FA up to 20 kPa at 303 K.

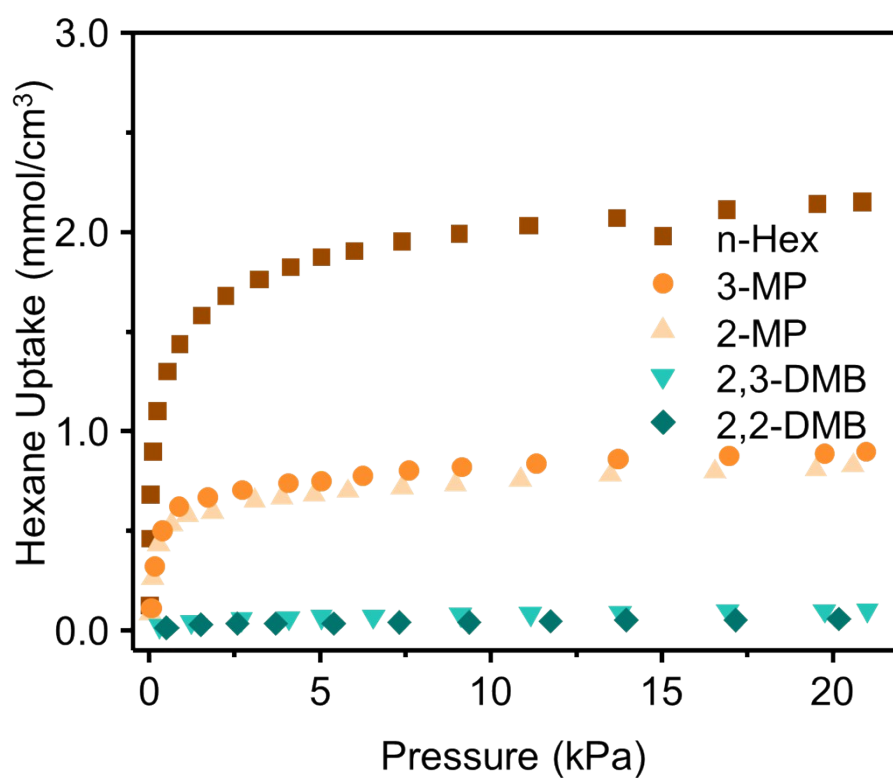


Figure S19. Single-component hexane isomer vapor isotherms on Hf-fum-FA up to 20 kPa at 333 K.

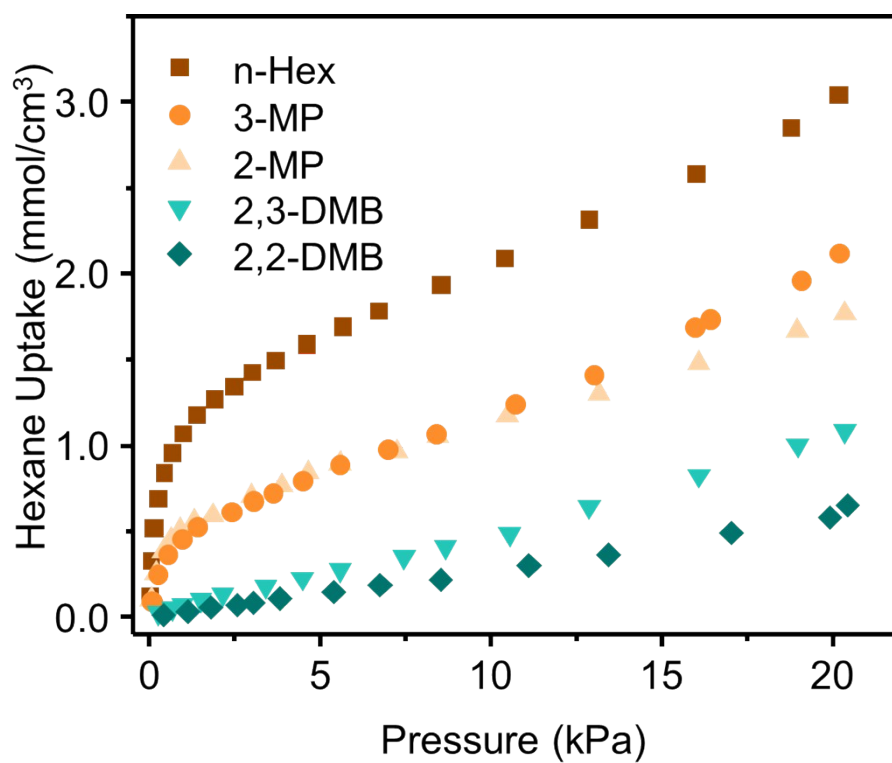


Figure S20. Single-component hexane isomer vapor isotherms on Hf-fum-FA up to 20 kPa at 363 K.

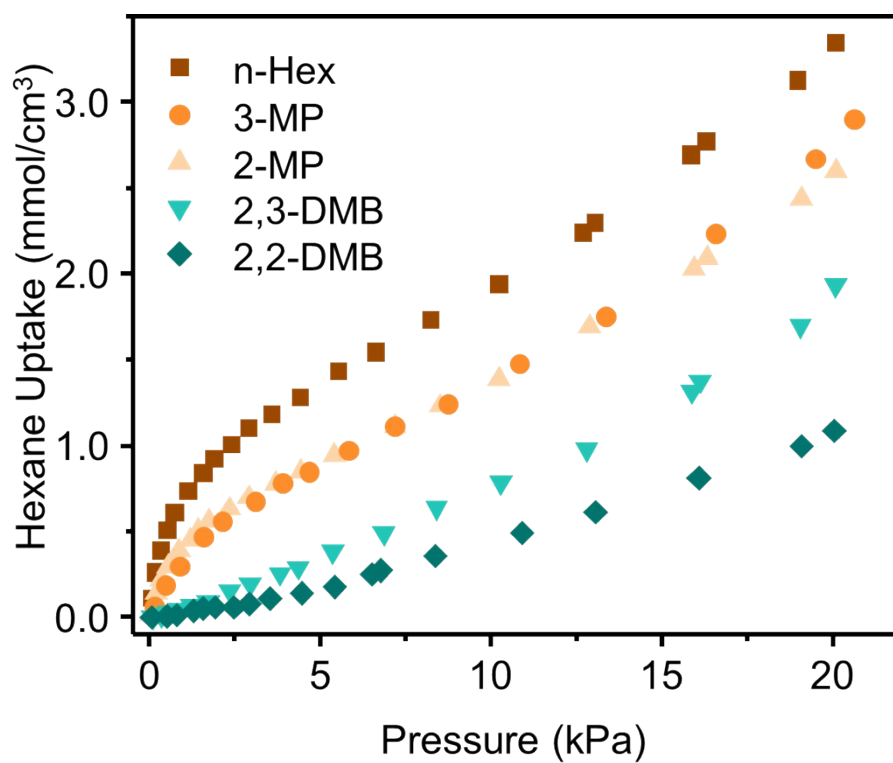


Figure S21. Single-component hexane isomer vapor isotherms on Hf-fum-FA up to 20 kPa at 393 K.

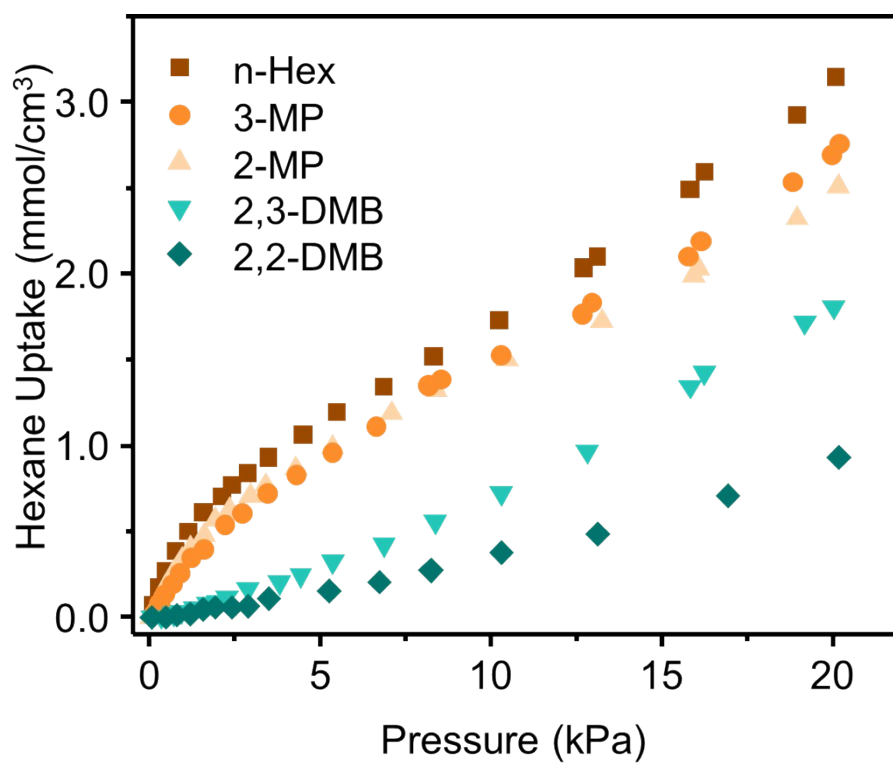


Figure S22. Single-component hexane isomer vapor isotherms on Hf-fum-FA up to 20 kPa at 423 K.

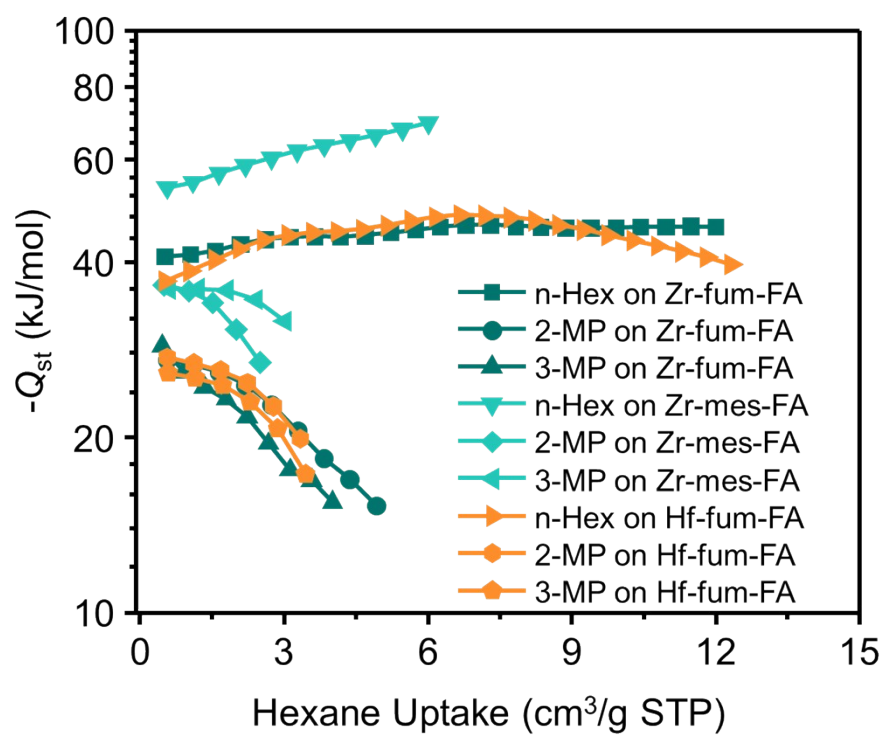


Figure S23. The isosteric heats of adsorption of hexane isomers on Zr-fum-FA, Zr-mes-FA, and Hf-fum-FA, calculated with the Clausius-Clapeyron equation.

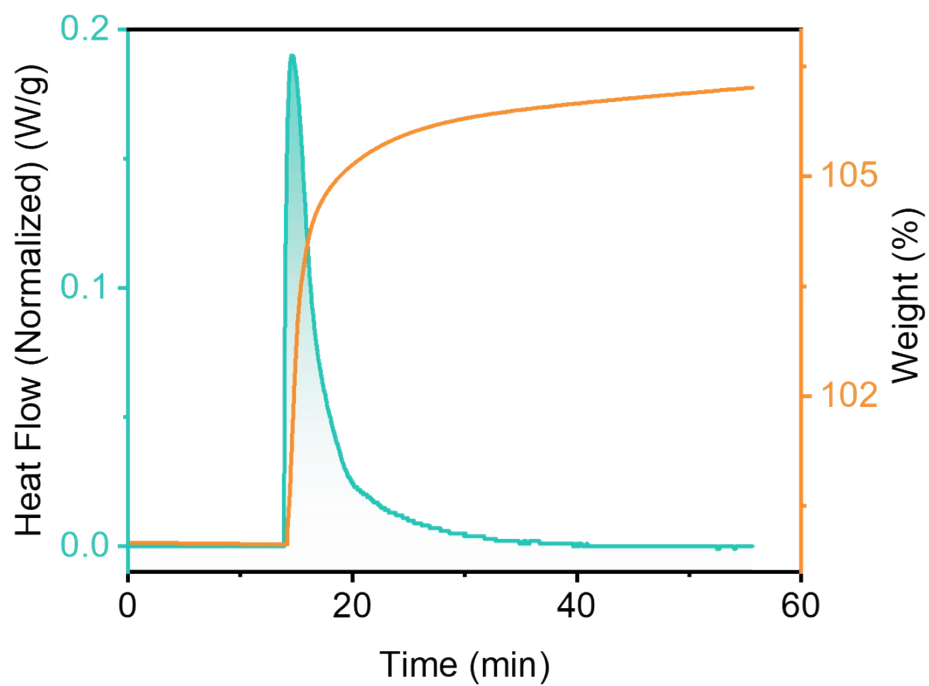


Figure S24. The TG-DSC measurement of n-Hex adsorption on Zr-fum-FA at 303 K, 15 kPa.

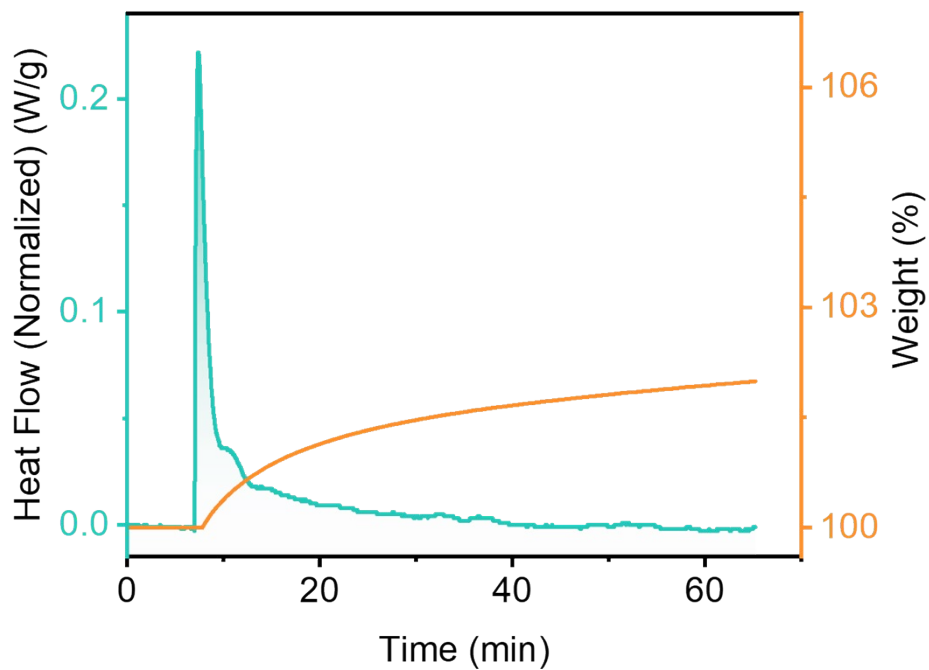


Figure S25. The TG-DSC measurement of 3-MP adsorption on Zr-fum-FA at 303 K, 15 kPa.

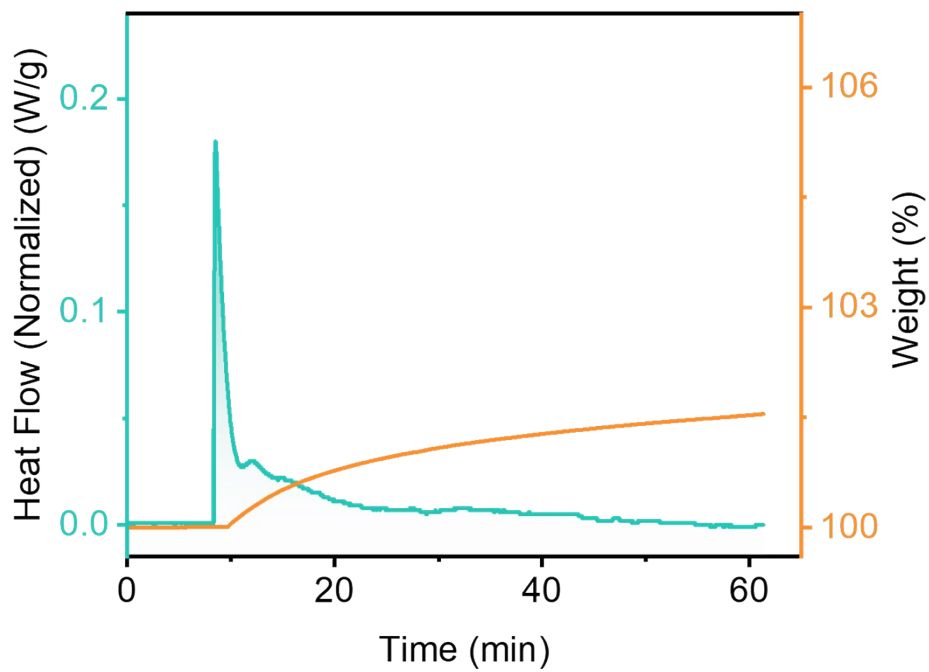


Figure S26. The TG-DSC measurement of 2-MP adsorption on Zr-fum-FA at 303 K, 15 kPa.

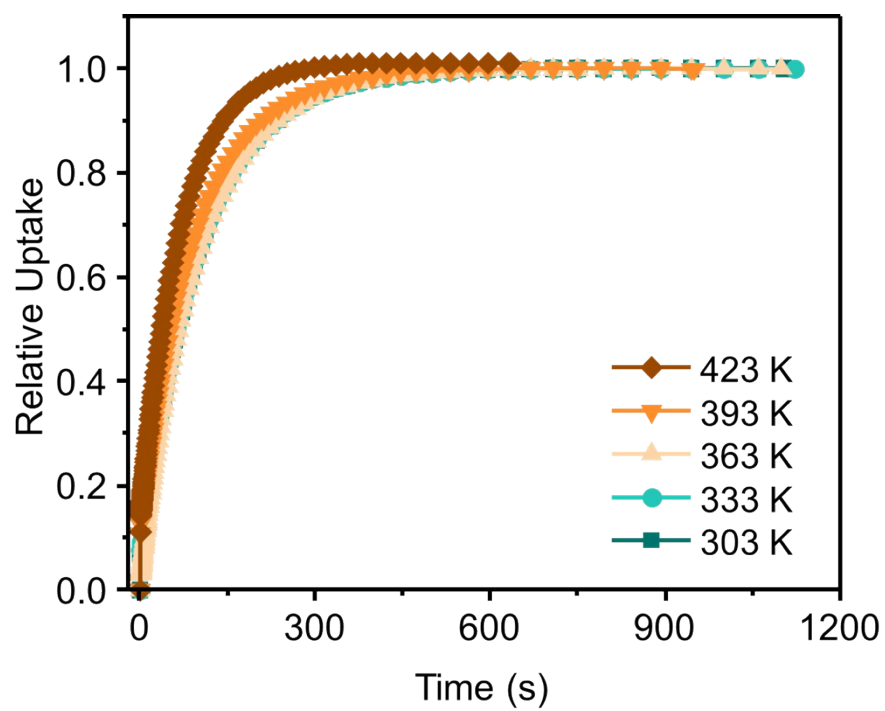


Figure S27. Time-dependent relative adsorption amounts of n-Hex on Zr-fum-FA at varied temperatures.

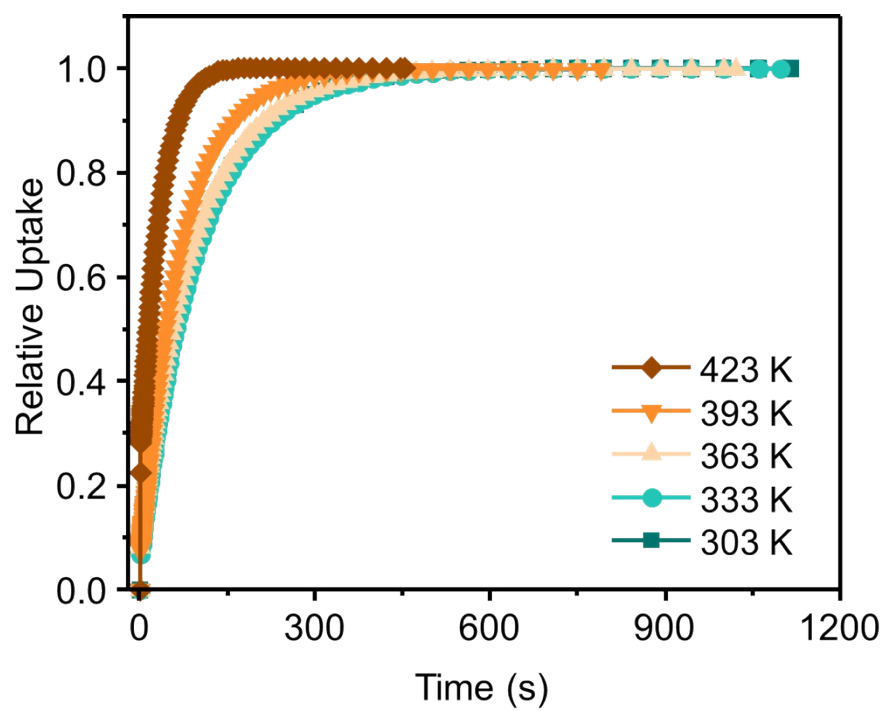


Figure S28. Time-dependent relative adsorption amounts of n-Hex on Zr-mes-FA at varied temperatures.

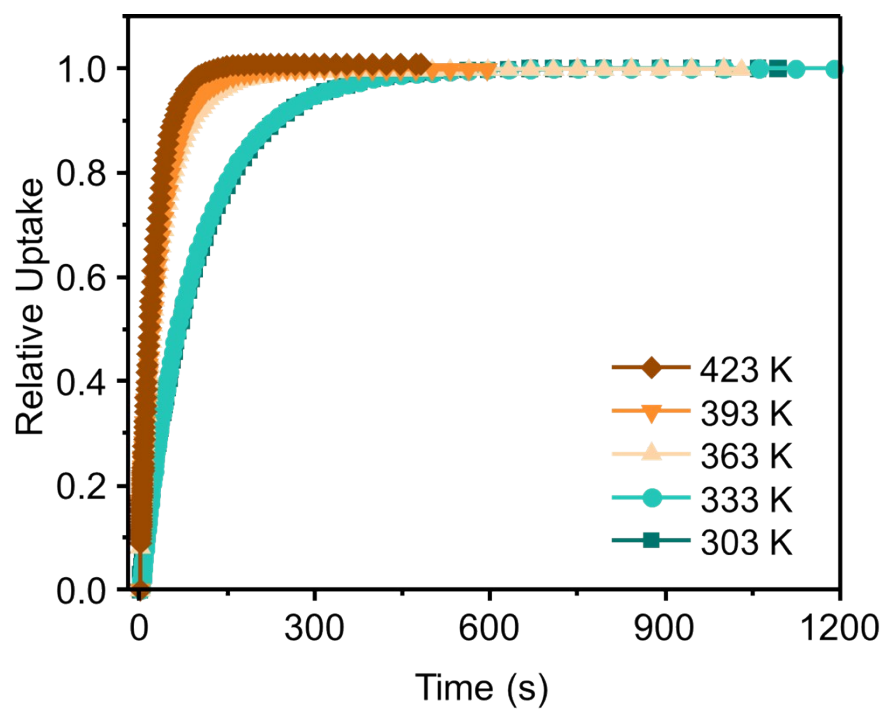


Figure S29. Time-dependent relative adsorption amounts of n-Hex on Hf-fum-FA at varied temperatures.

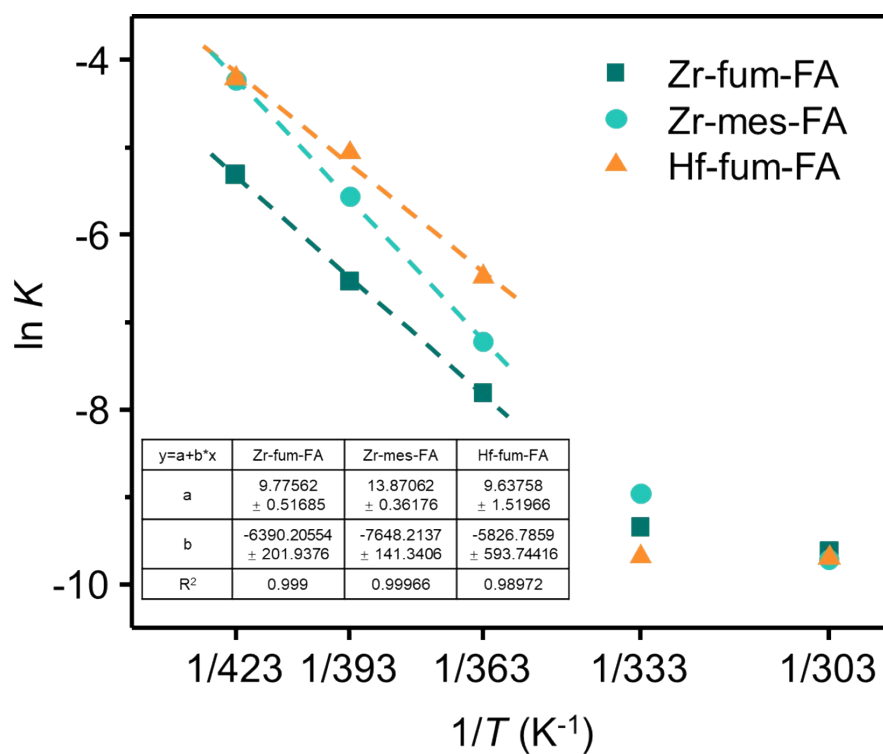


Figure S30. The relationship between the mass-transfer coefficients of n-Hex and temperatures on Zr-fum-FA, Zr-mes-FA, and Hf-fum-FA, respectively.

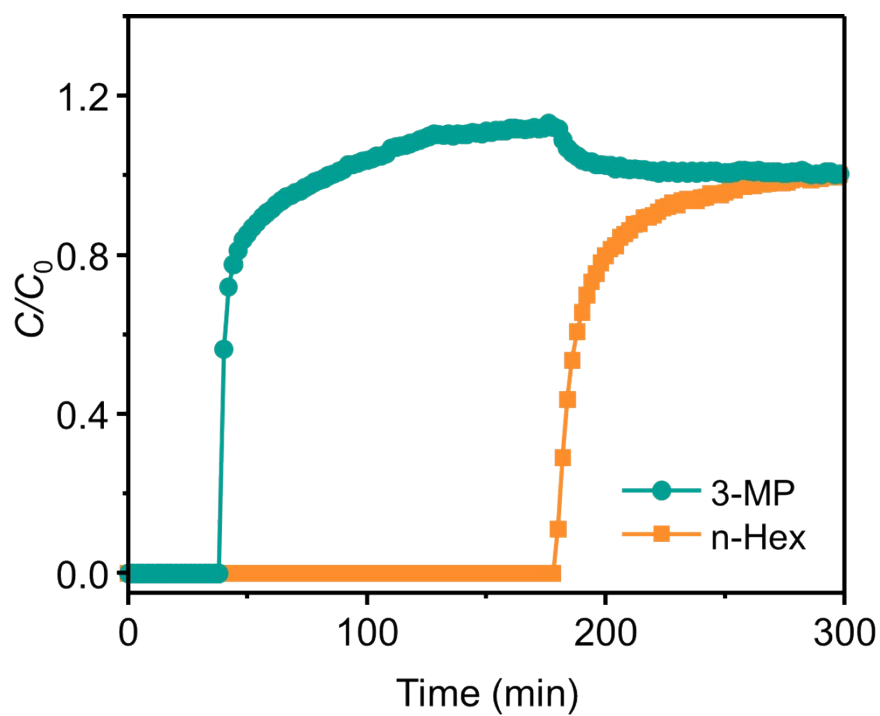


Figure S31. The binary equimolar breakthrough curves of n-Hex/3-MP at 303 K on a column packed with Zr-fum-FA.

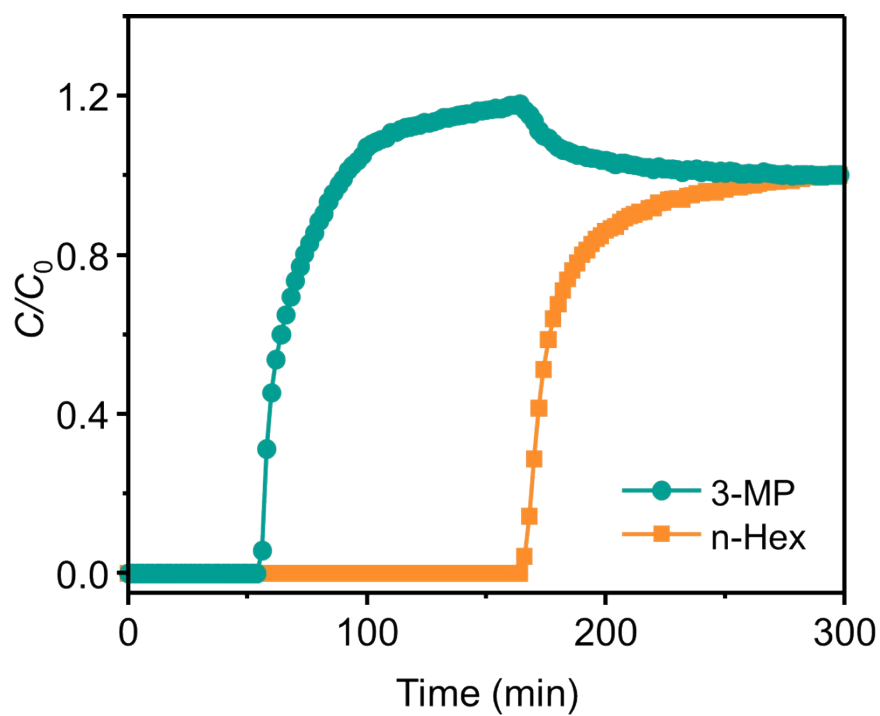


Figure S32. The binary equimolar breakthrough curves of n-Hex/3-MP at 333 K on a column packed with Zr-fum-FA.

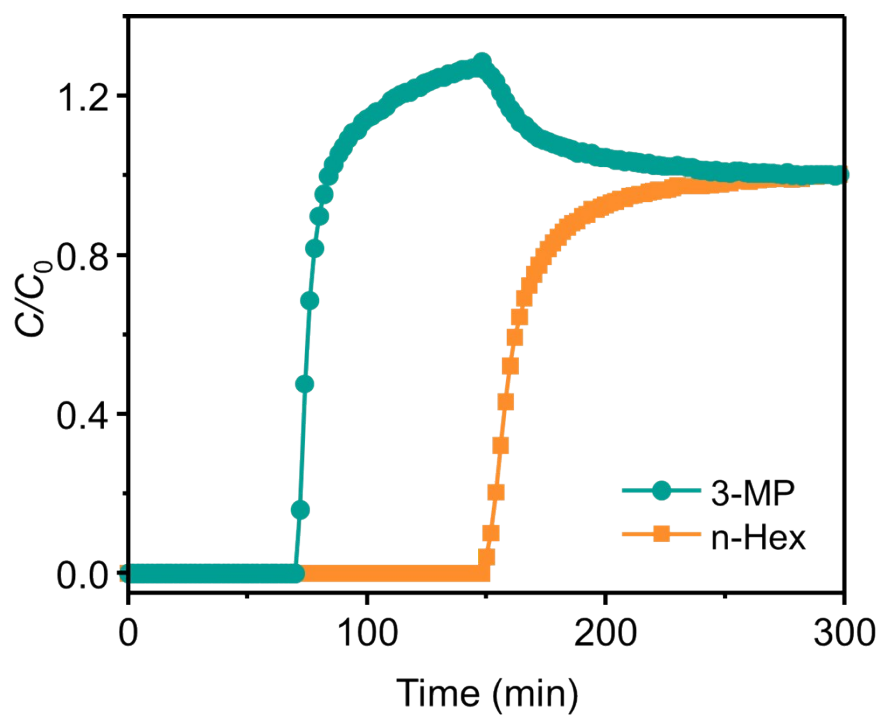


Figure S33. The binary equimolar breakthrough curves of n-Hex/3-MP at 363 K on a column packed with Zr-fum-FA.

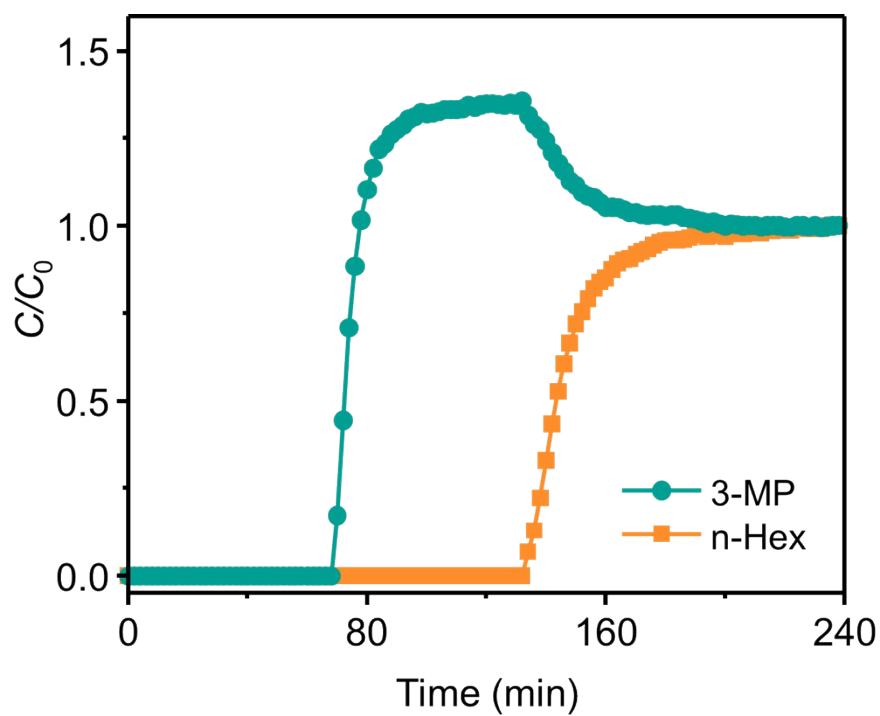


Figure S34. The binary equimolar breakthrough curves of n-Hex/3-MP at 393 K on a column packed with Zr-fum-FA.

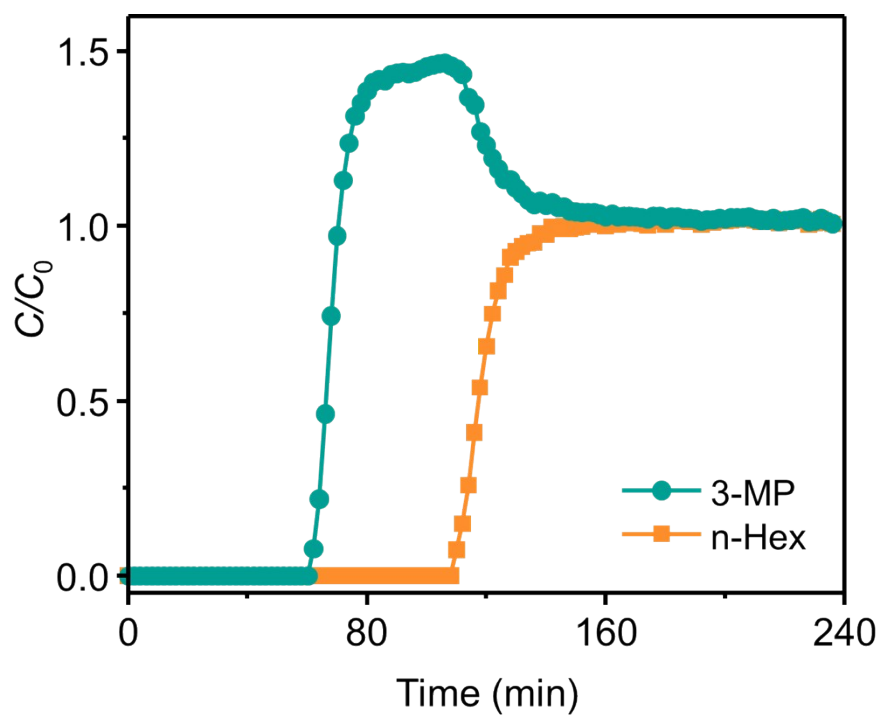


Figure S35. The binary equimolar breakthrough curves of n-Hex/3-MP at 423 K on a column packed with Zr-fum-FA.

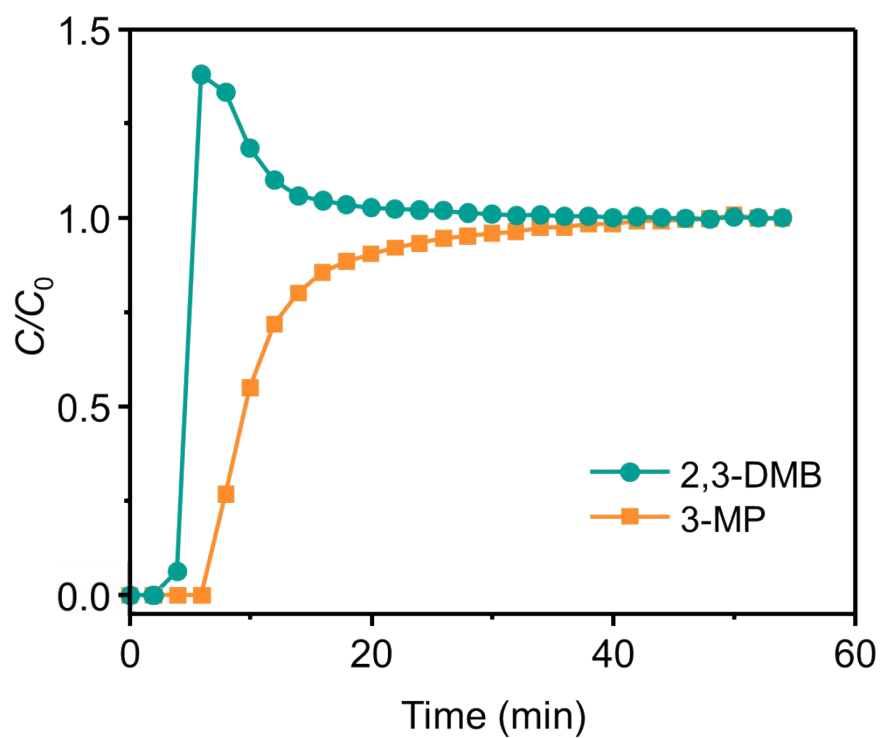


Figure S36. The binary equimolar breakthrough curves of 3-MP/2,3-DMB at 303 K on a column packed with Zr-fum-FA.

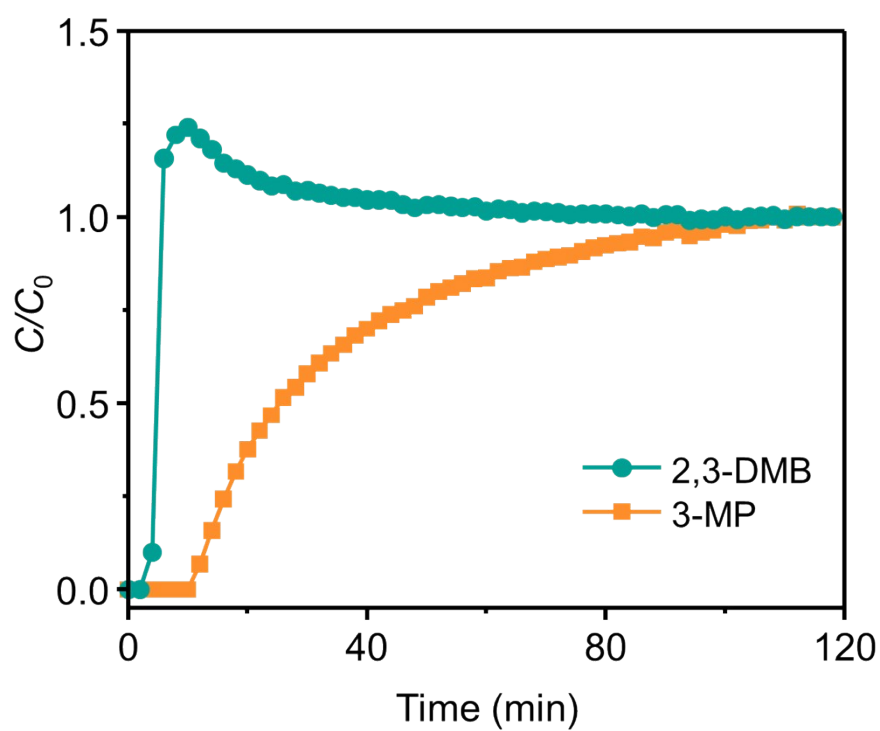


Figure S37. The binary equimolar breakthrough curves of 3-MP/2,3-DMB at 333 K on a column packed with Zr-fum-FA.

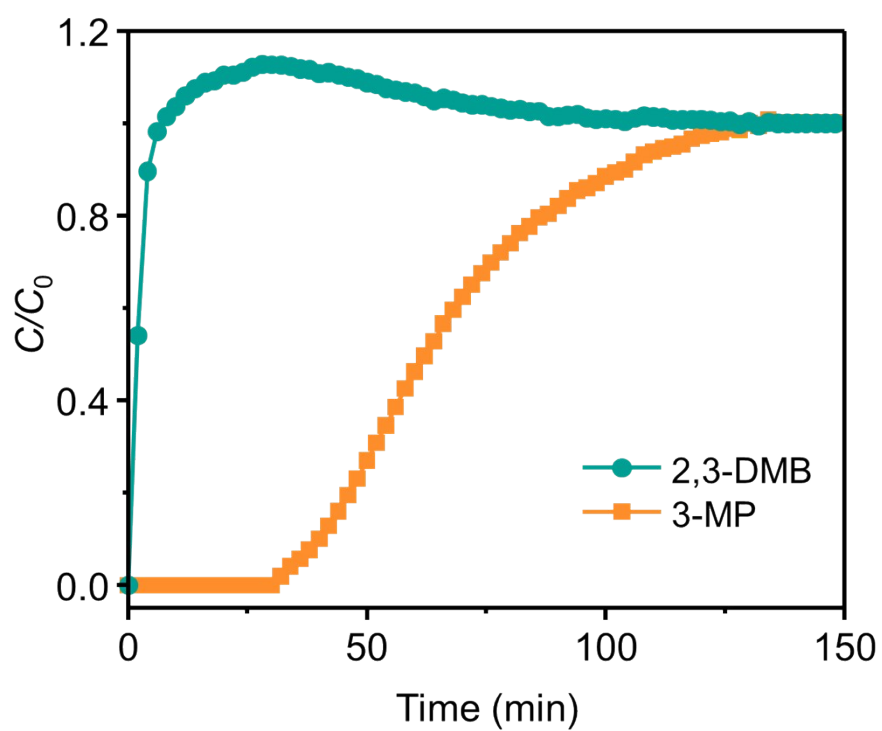


Figure S38. The binary equimolar breakthrough curves of 3-MP/2,3-DMB at 363 K on a column packed with Zr-fum-FA.

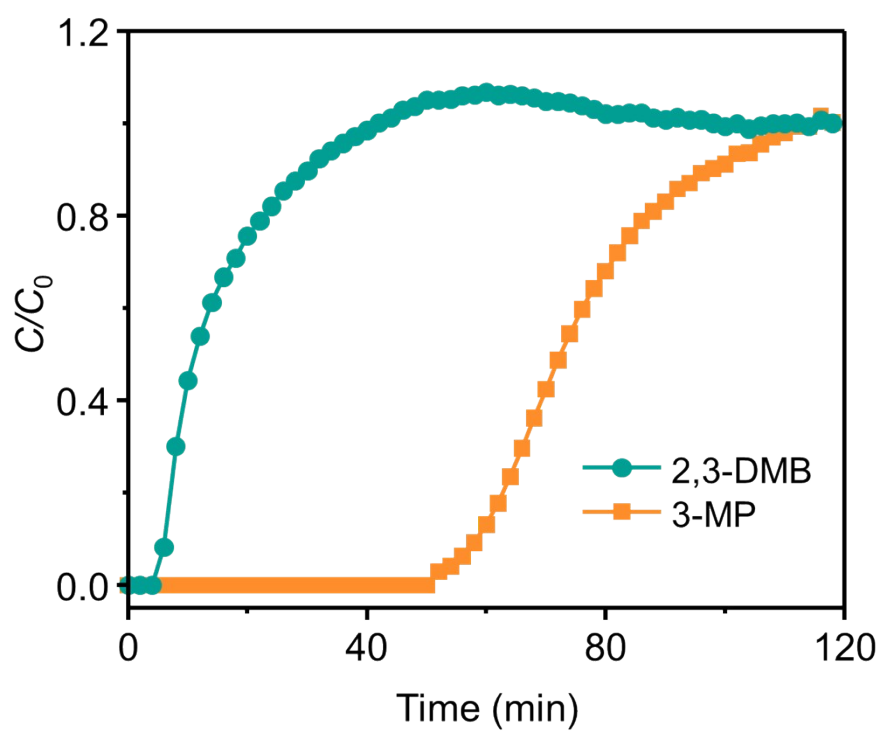


Figure S39. The binary equimolar breakthrough curves of 3-MP/2,3-DMB at 393 K on a column packed with Zr-fum-FA.

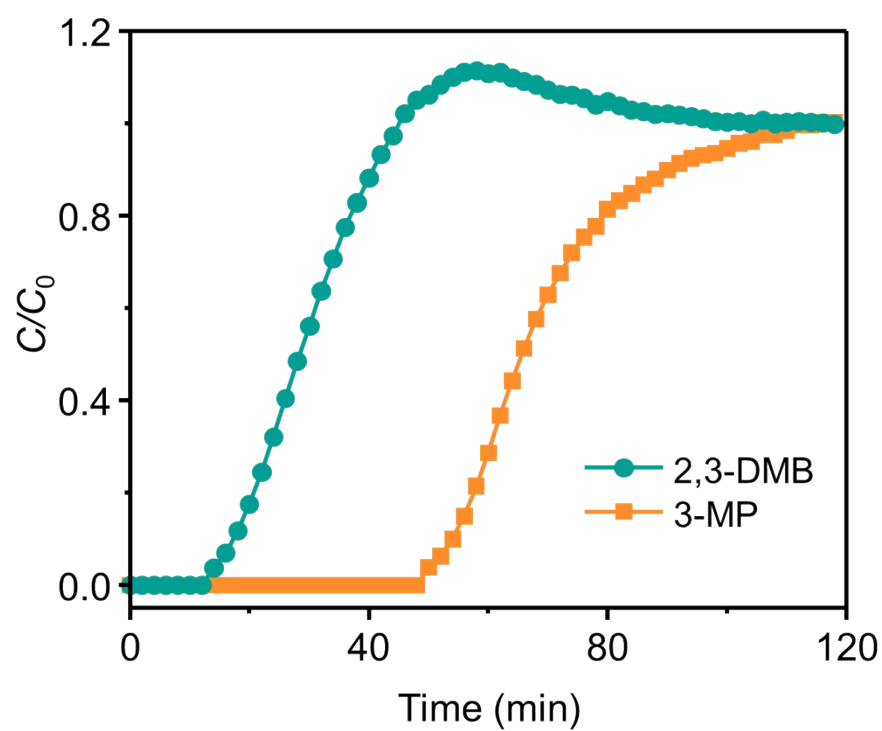


Figure S40. The binary equimolar breakthrough curves of 3-MP/2,3-DMB at 423 K on a column packed with Zr-fum-FA.

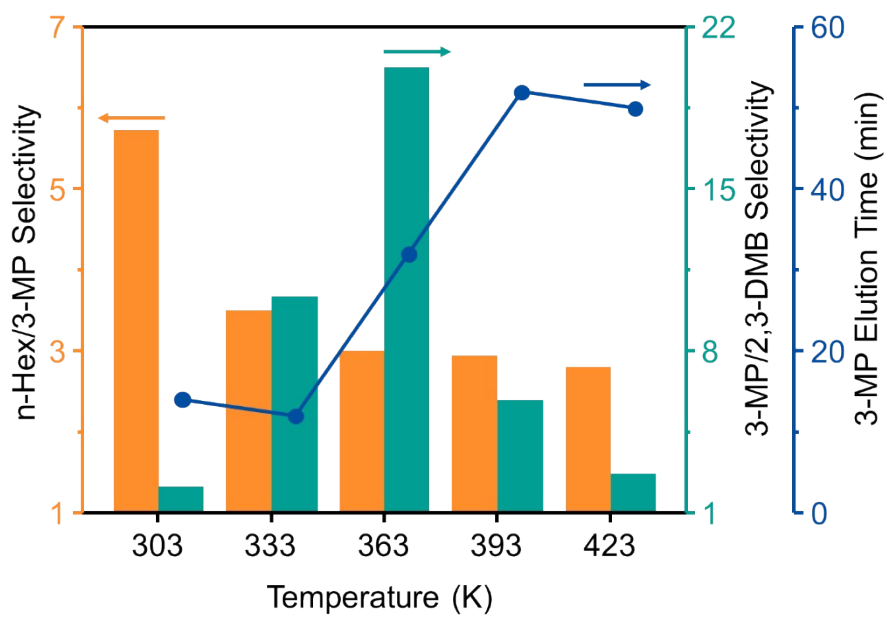


Figure S41. The binary breakthrough selectivity of n-Hex/3-MP and 3-MP/2,3-DMB on Zr-fum-FA, and 3-MP elution time in 3-MP/2,3-DMB breakthrough experiments.

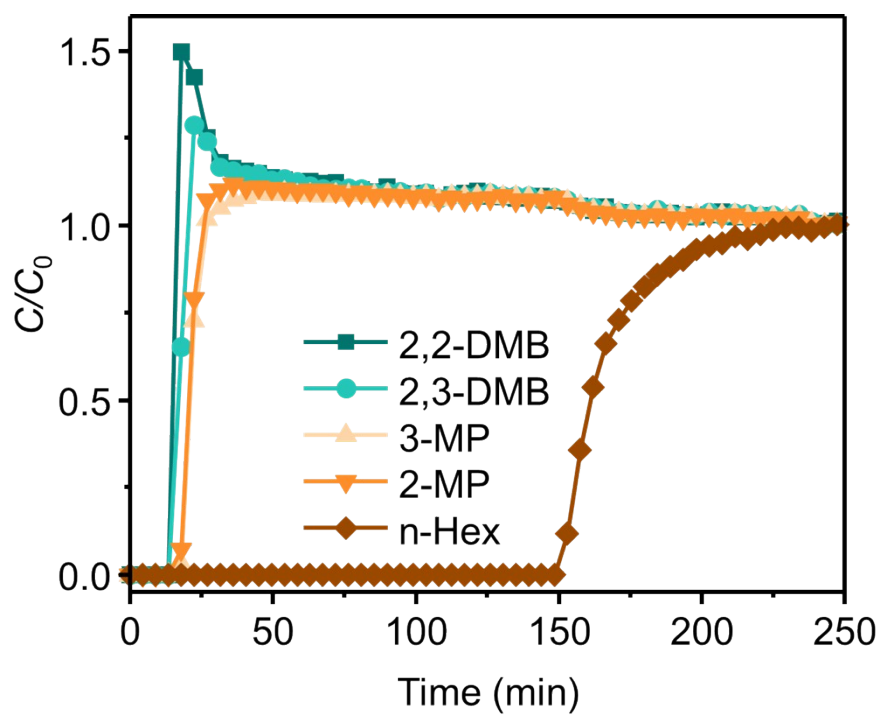


Figure S42. The quinary equimolar breakthrough curves of all hexane isomers on Zr-fum-FA at 303 K.

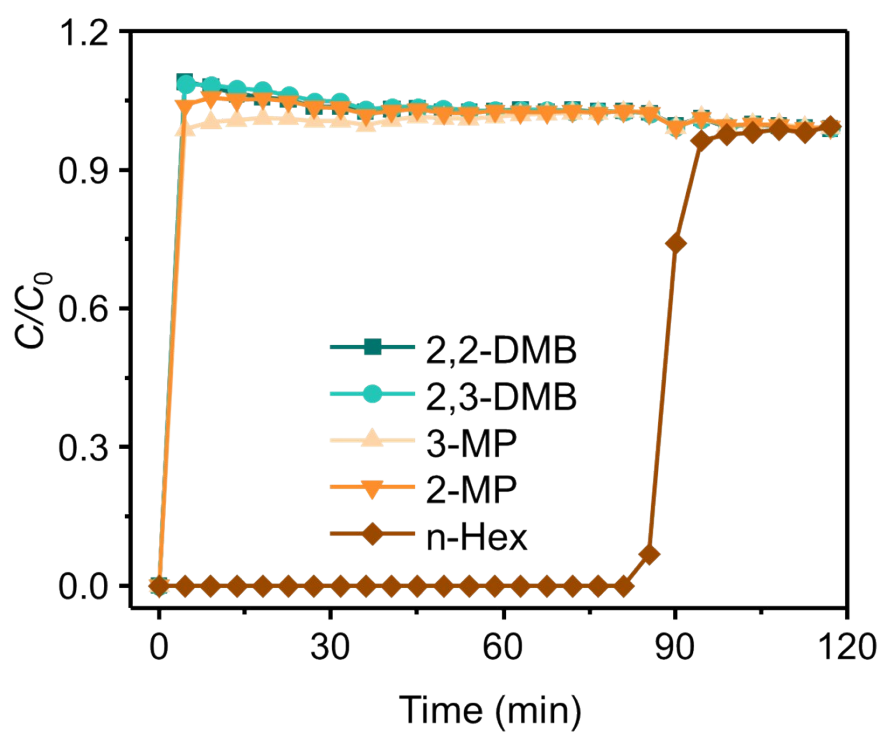


Figure S43. The quinary equimolar breakthrough curves of all hexane isomers on Zr-mes-FA at 303 K.

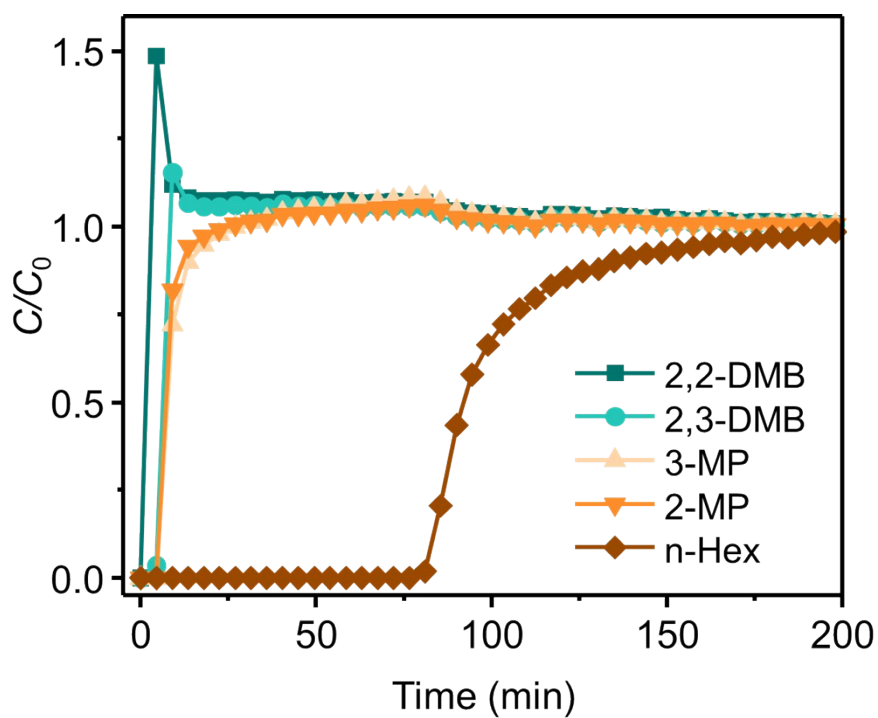


Figure S44. The quinary equimolar breakthrough curves of all hexane isomers on Hf-fum-FA at 303 K.

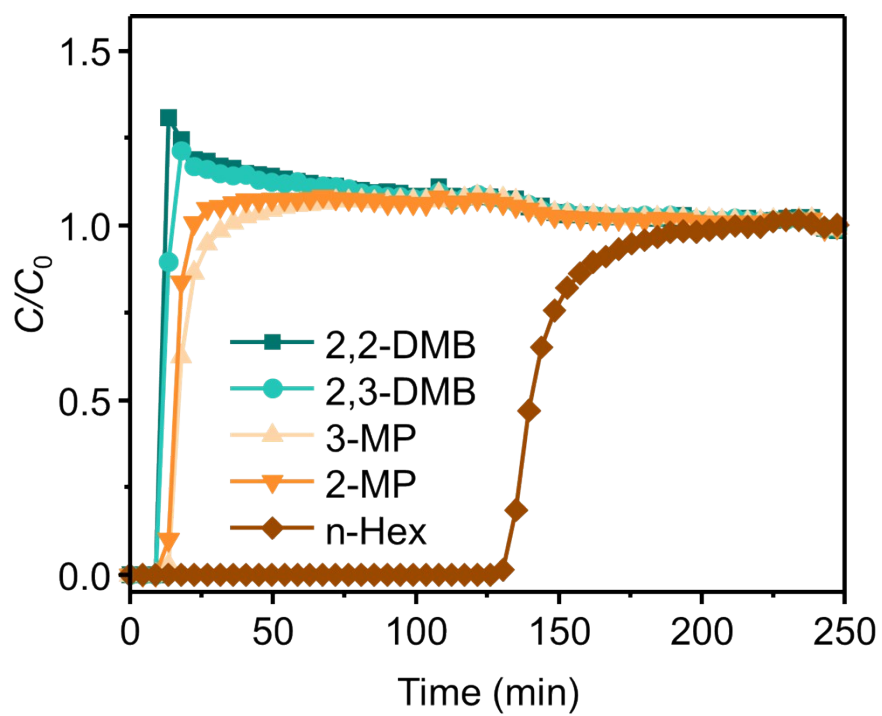


Figure S45. The quinary equimolar breakthrough curves of all hexane isomers on Zr-fum-FA at 333 K.

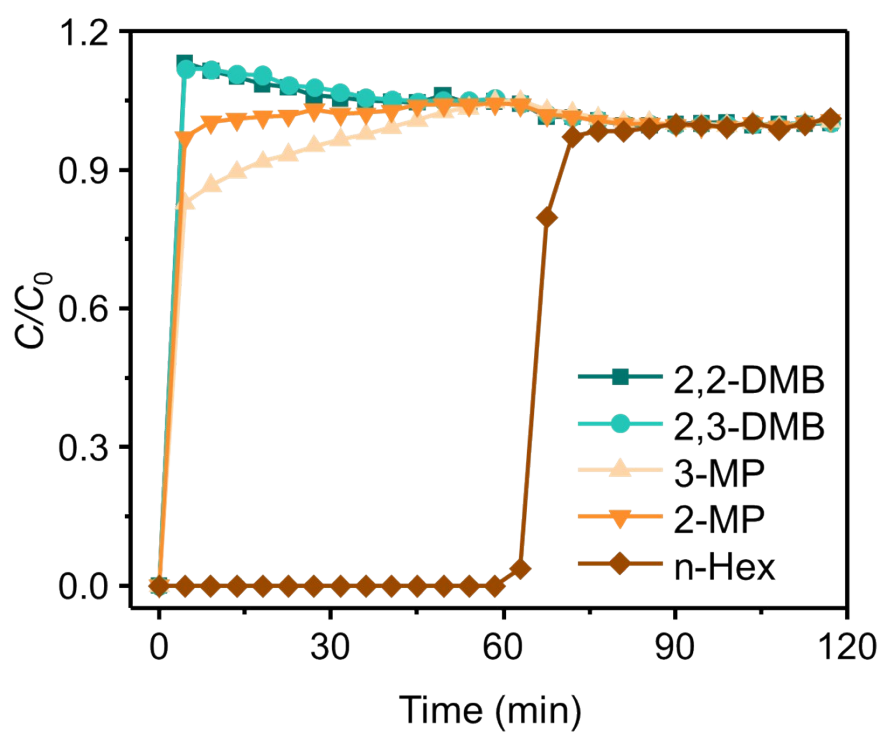


Figure S46. The quinary equimolar breakthrough curves of all hexane isomers on Zr-mes-FA at 333 K.

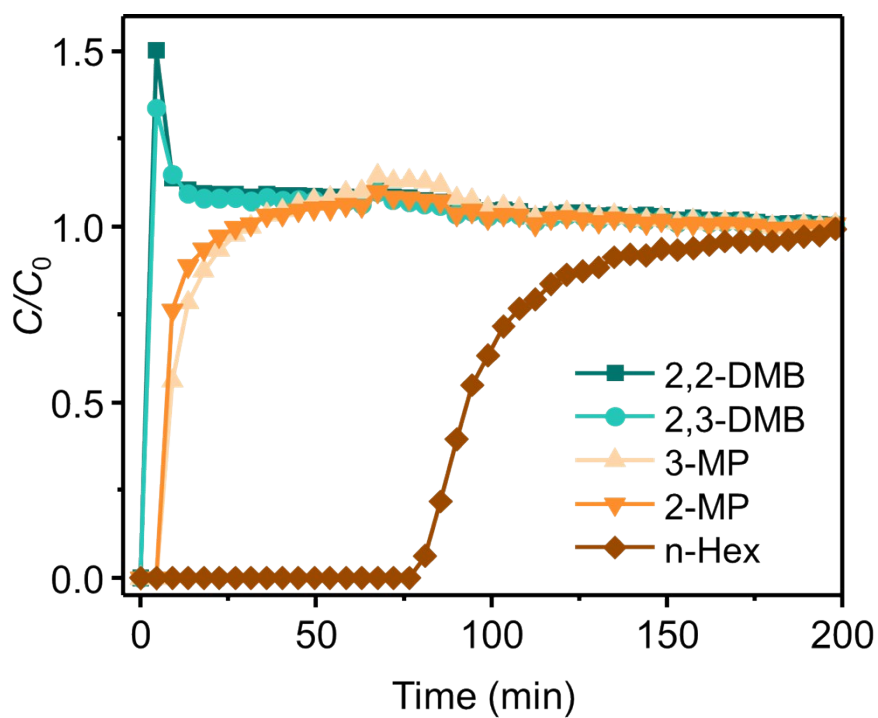


Figure S47. The quinary equimolar breakthrough curves of all hexane isomers on Hf-fum-FA at 333 K.

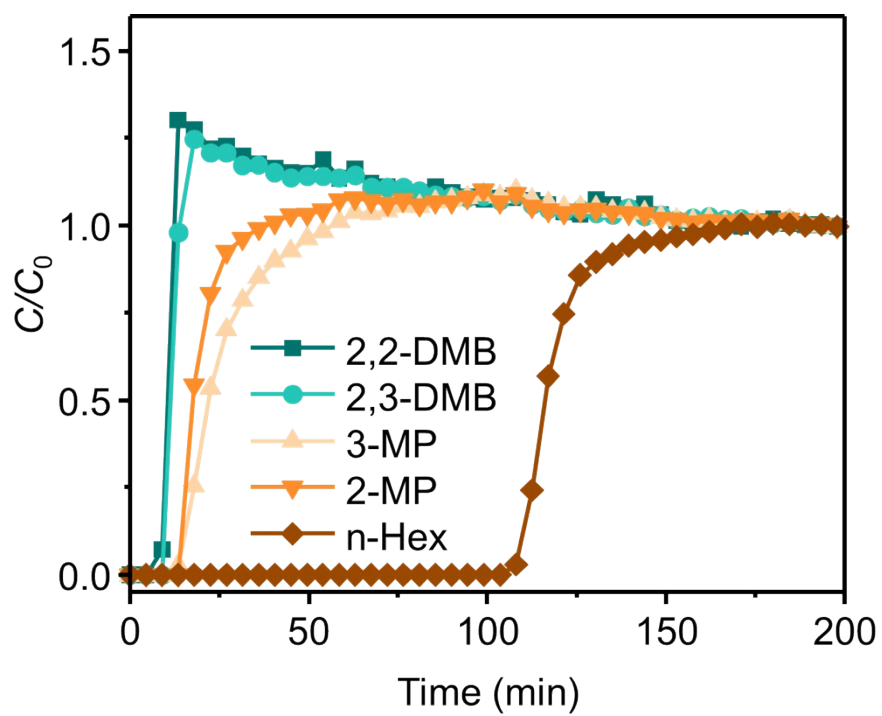


Figure S48. The quinary equimolar breakthrough curves of all hexane isomers on Zr-fum-FA at 363 K.

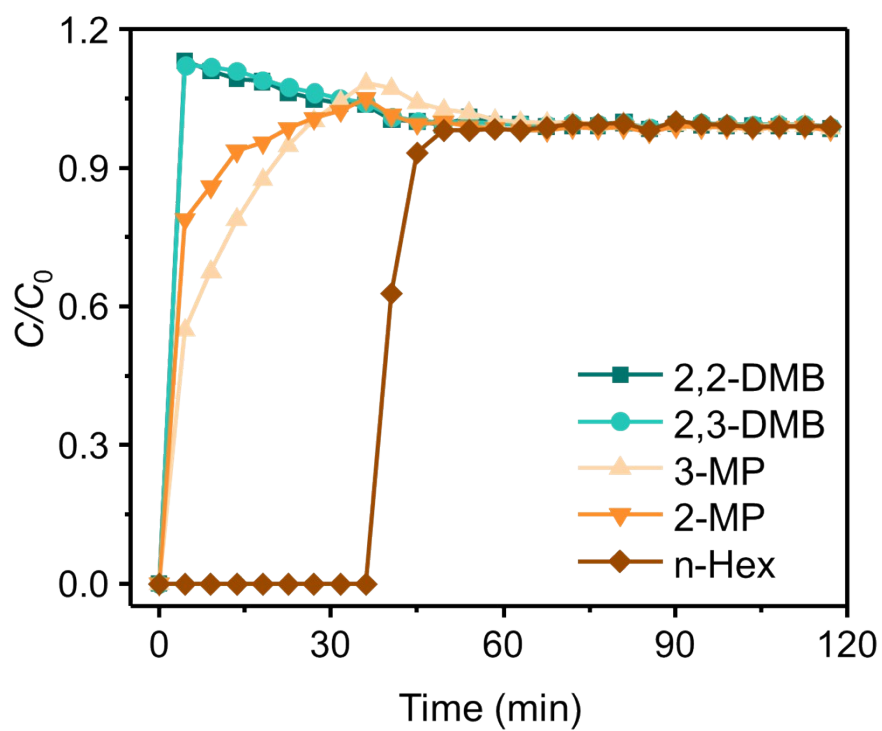


Figure S49. The quinary equimolar breakthrough curves of all hexane isomers on Zr-mes-FA at 363 K.

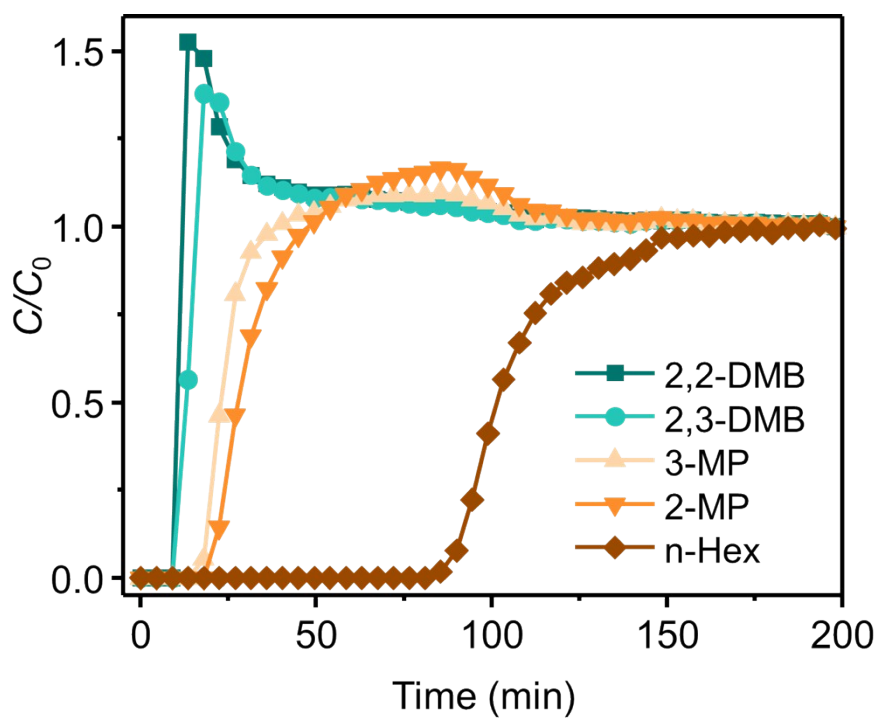


Figure S50. The quinary equimolar breakthrough curves of all hexane isomers on Hf-fum-FA at 363 K.

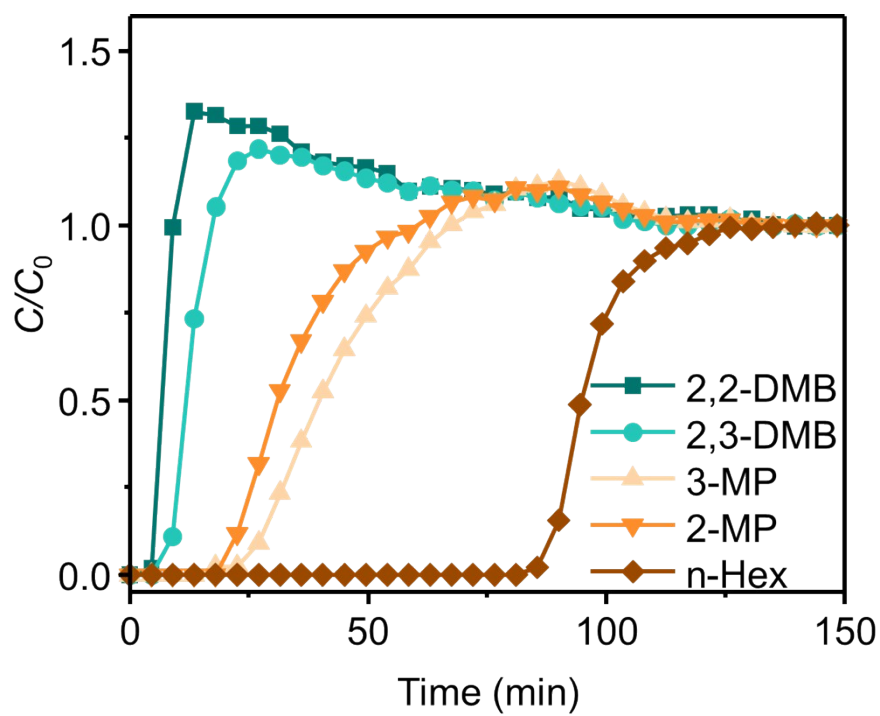


Figure S51. The quinary equimolar breakthrough curves of all hexane isomers on Zr-fum-FA at 393 K.

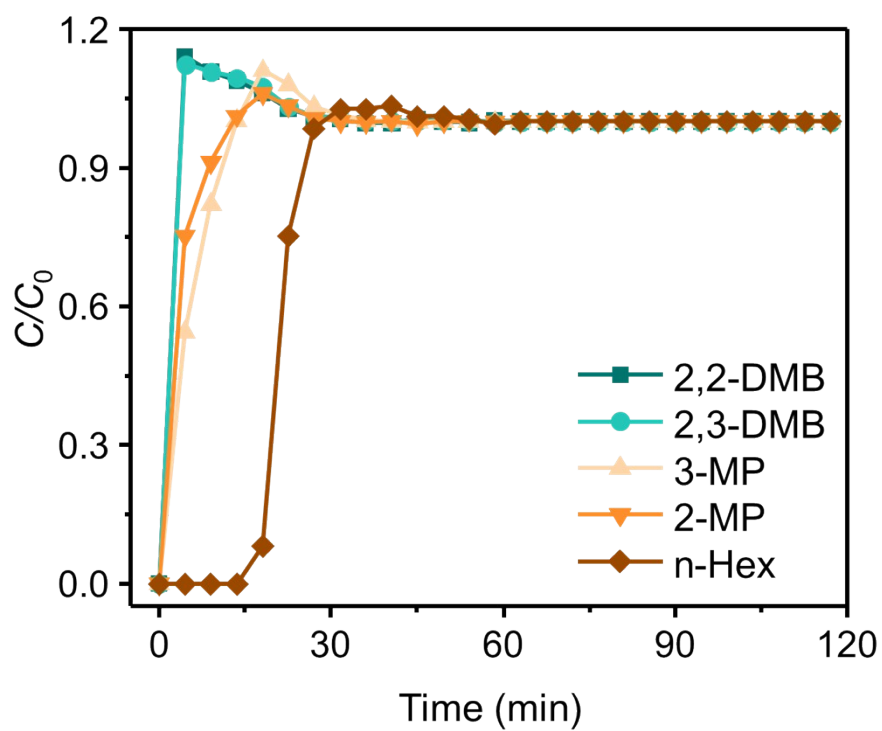


Figure S52. The quinary equimolar breakthrough curves of all hexane isomers on Zr-mes-FA at 393 K.

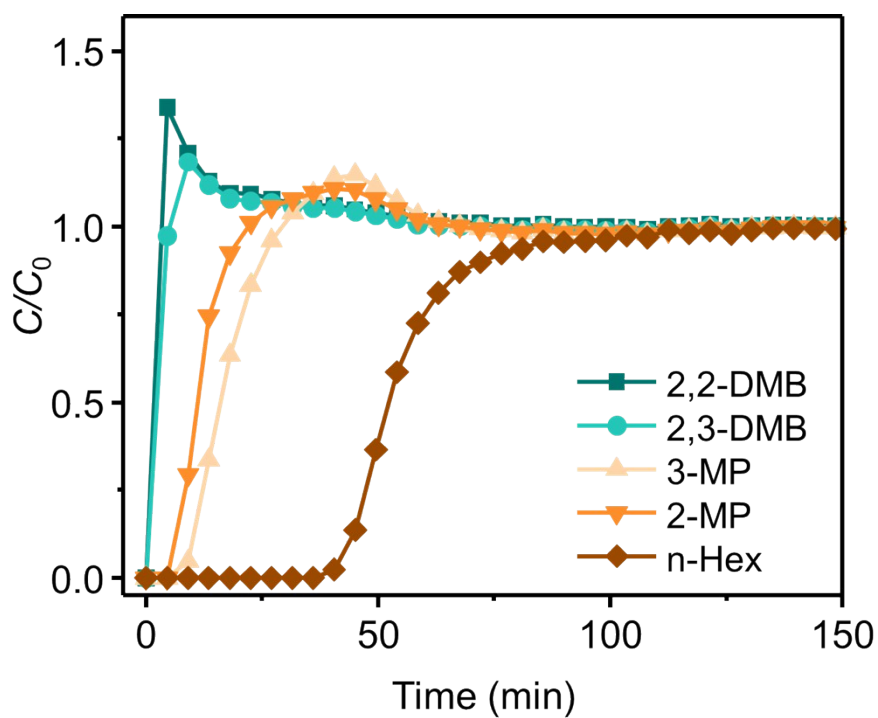


Figure S53. The quinary equimolar breakthrough curves of all hexane isomers on Hf-fum-FA at 393 K.

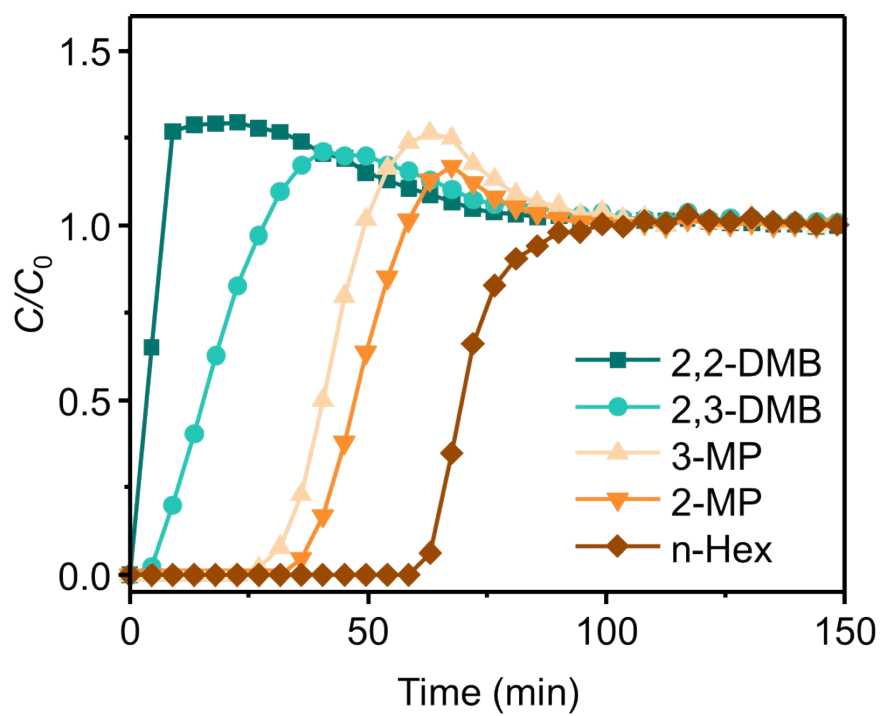


Figure S54. The quinary equimolar breakthrough curves of all hexane isomers on Zr-fum-FA at 423 K.

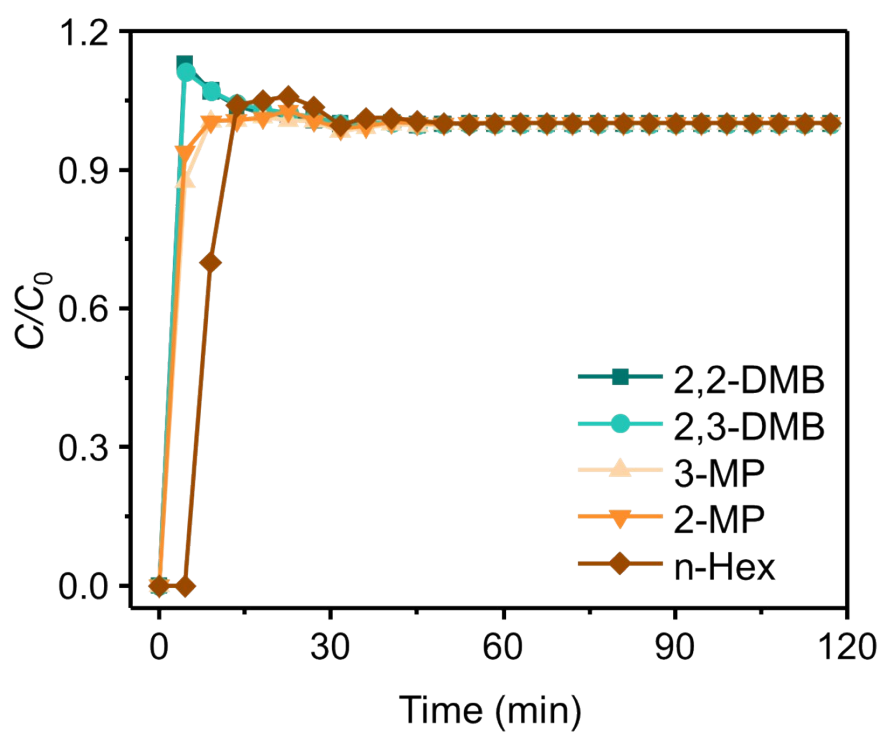


Figure S55. The quinary equimolar breakthrough curves of all hexane isomers on Zr-mes-FA at 423 K.

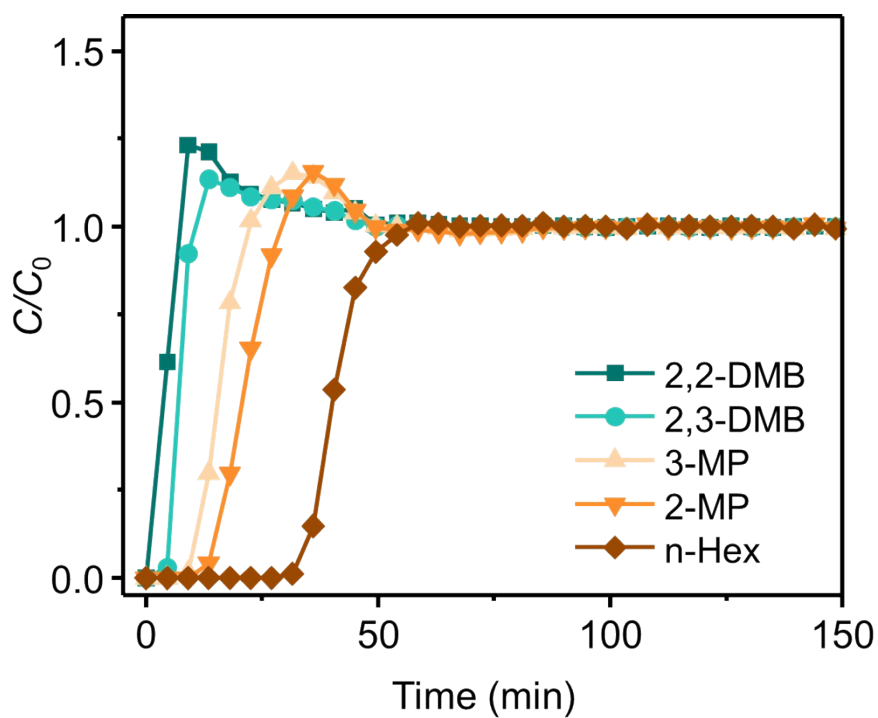


Figure S56. The quinary equimolar breakthrough curves of all hexane isomers on Hf-fum-FA at 423 K.

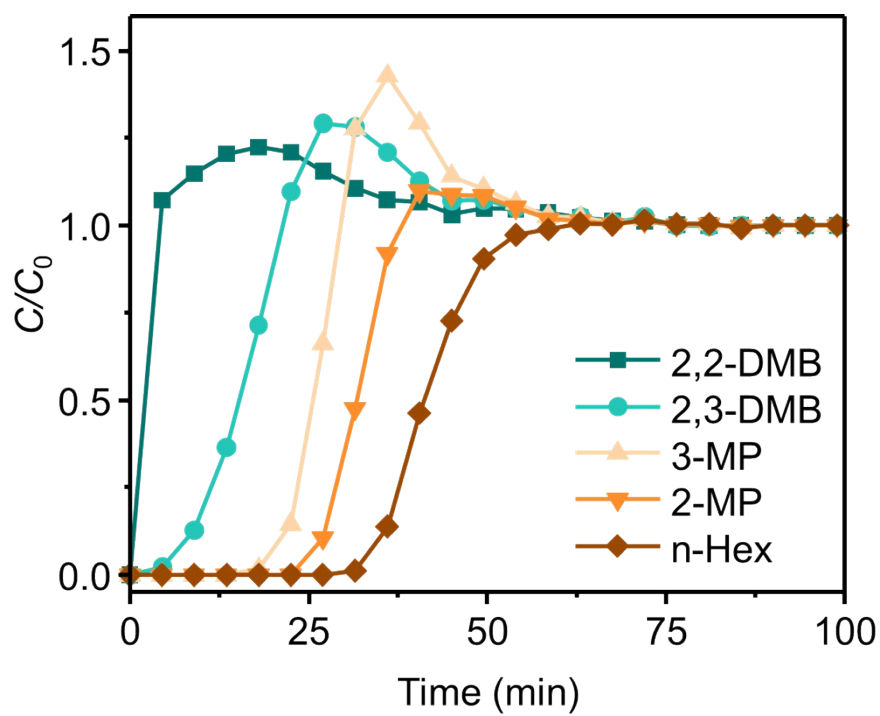


Figure S57. The quinary equimolar breakthrough curves of all hexane isomers on Zr-fum-FA at 453 K.

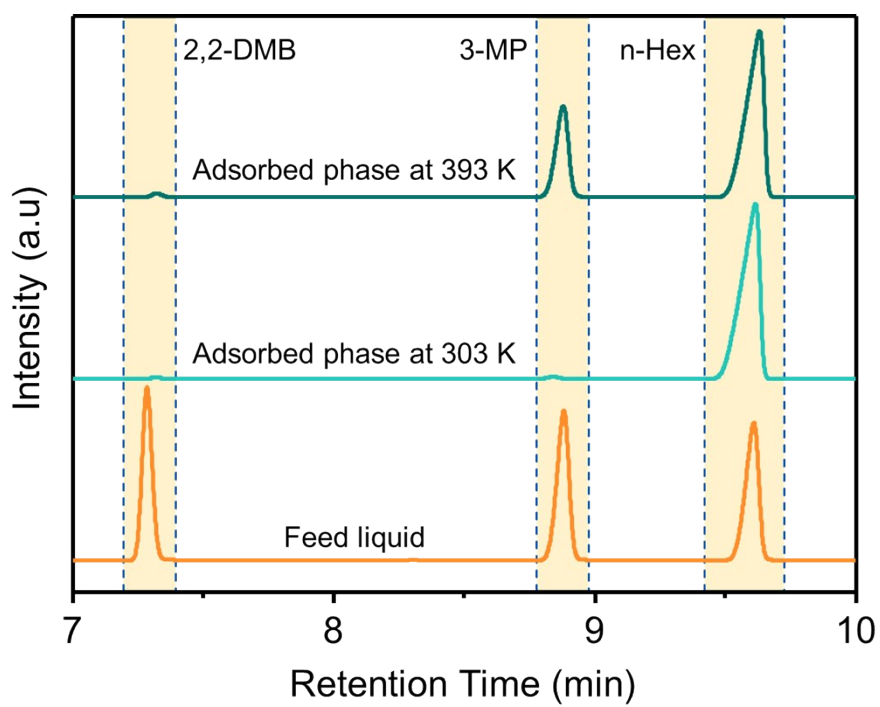


Figure S58. Liquid-phase adsorption of equimolar mixture of n-Hex, 3-MP, and 2,2-DMB on Zr-fum-FA at 303 and 393 K.

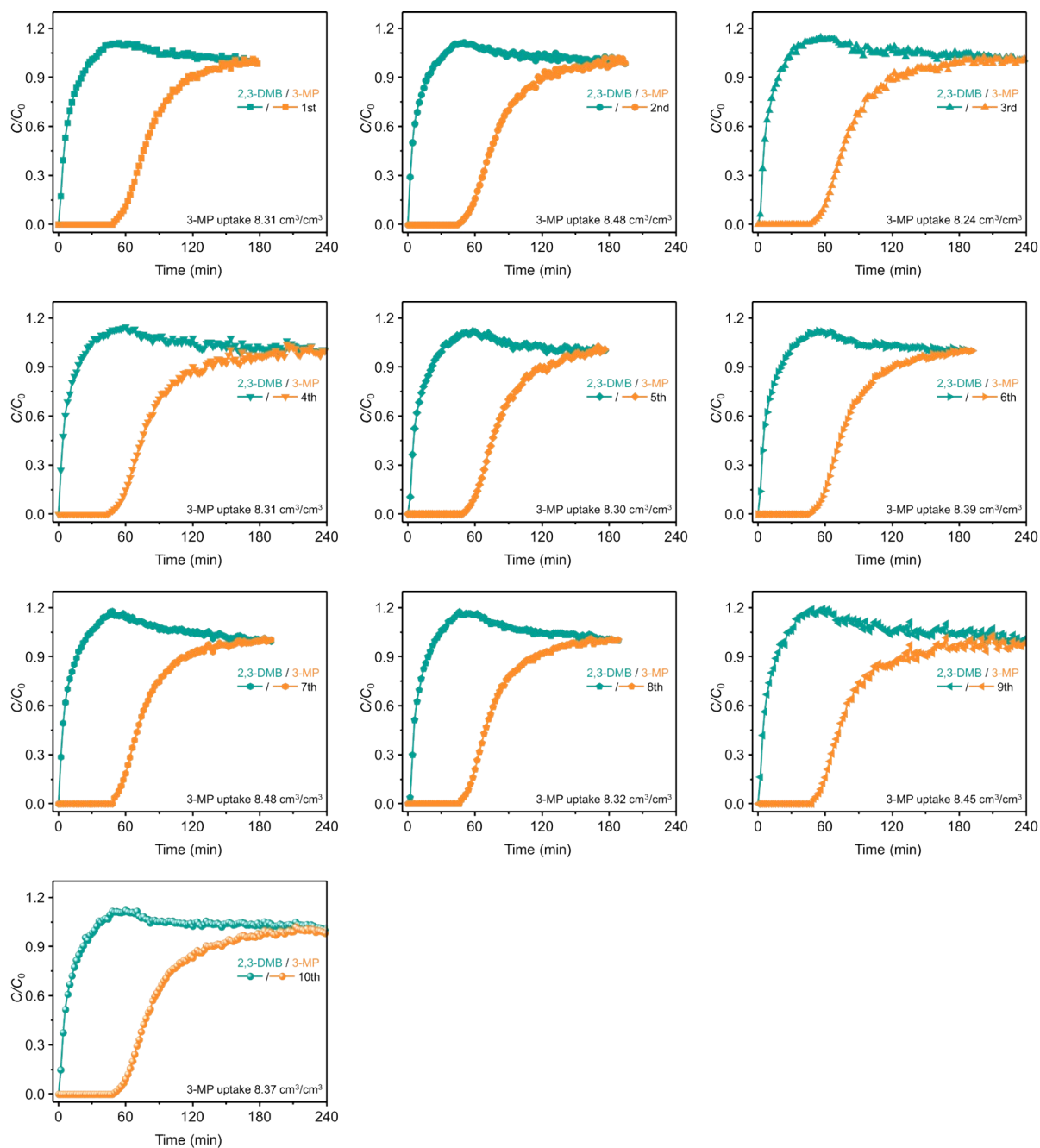


Figure S59. 10-Cycles equimolar binary breakthrough curves of 3-MP/2,3-DMB at 393 K on a column packed with Zr-fum-FA.

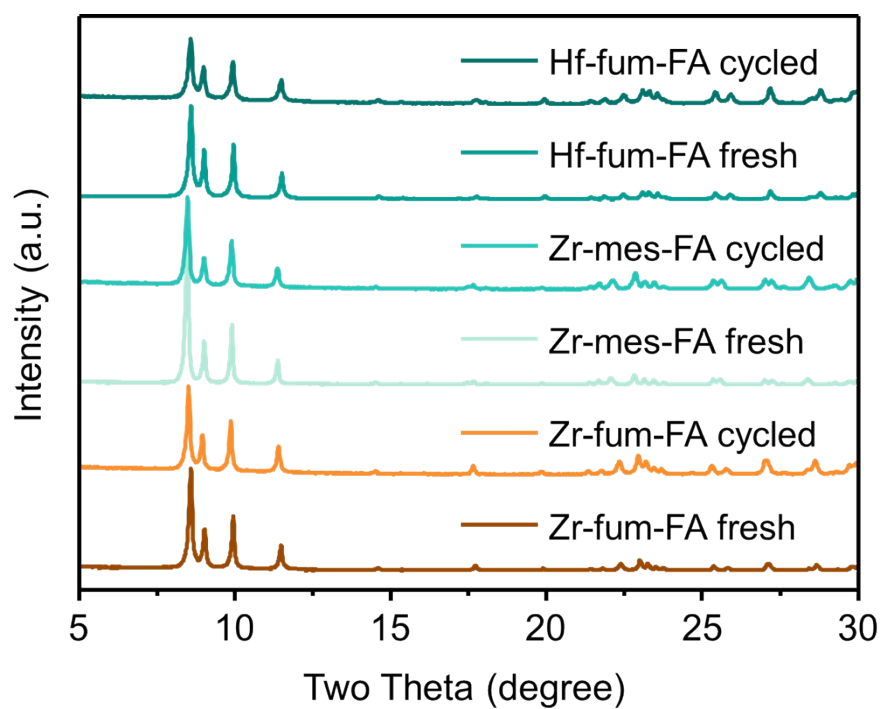


Figure S60. The PXRD patterns of as-synthesized Zr-fum-FA, Zr-mes-FA, and Hf-fum-FA, and corresponding samples after all hexane vapor adsorption-desorption tests.

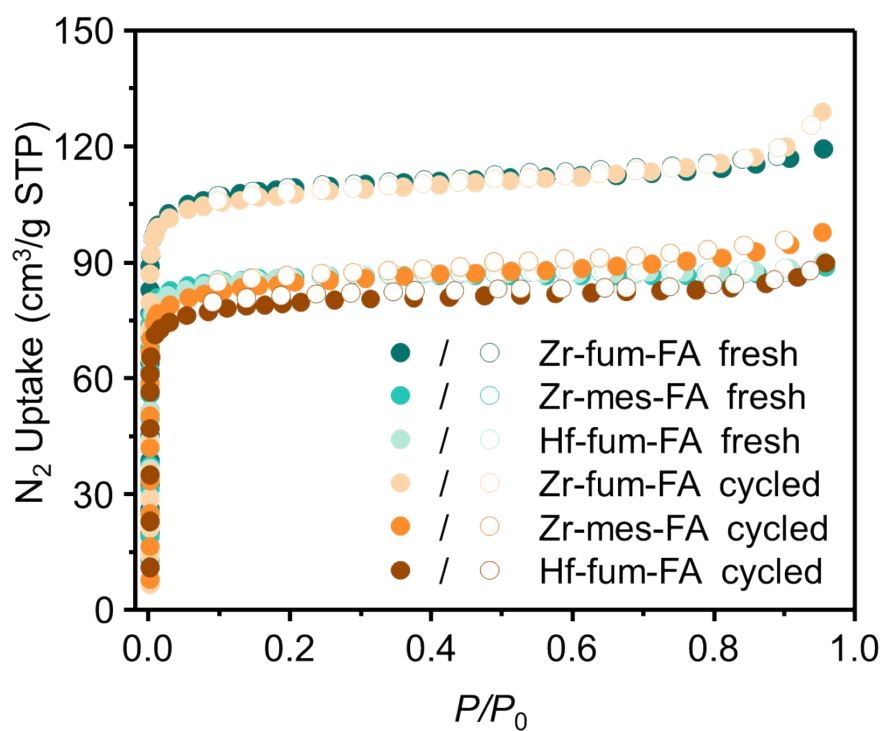


Figure S61. The N₂ adsorption-desorption isotherms at 77 K of as-synthesized Zr-fum-FA, Zr-mes-FA, and Hf-fum-FA, and corresponding samples after all hexane vapor adsorption-desorption tests.

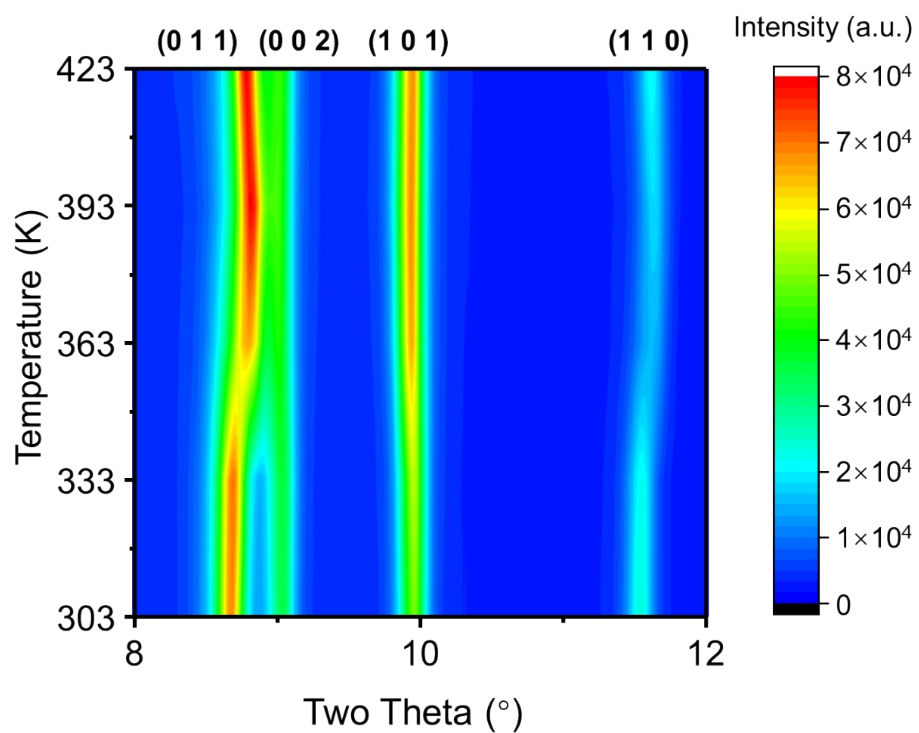


Figure S62. In-situ PXRD patterns of Zr-fum-FA under a pure N₂ flow with a temperature range of 303 to 423 K.

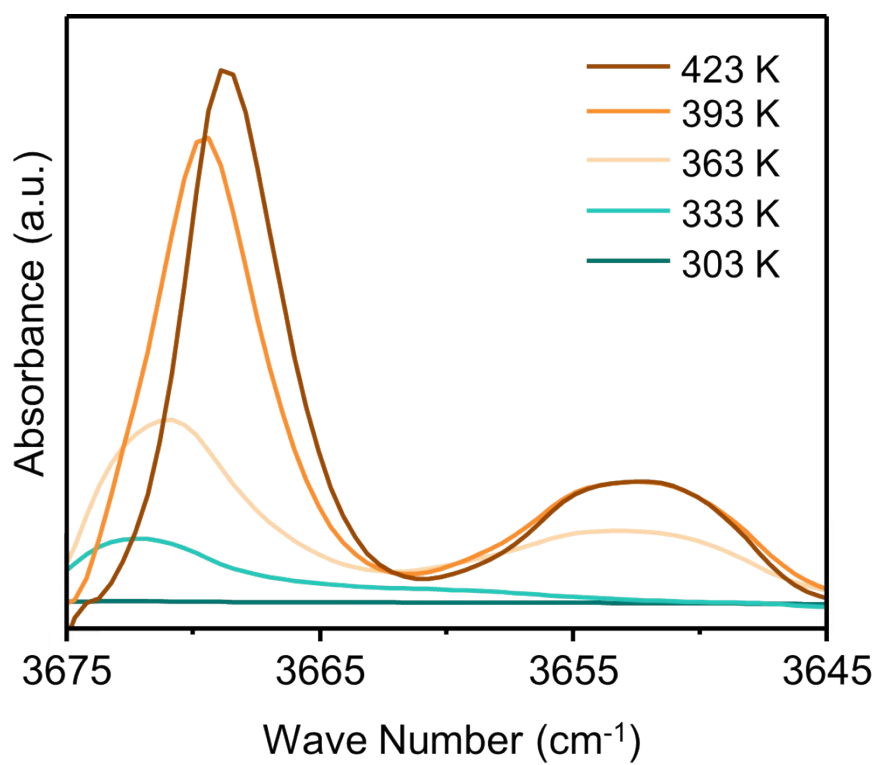


Figure S63. DRIFTS spectra of Zr-mes-FA under a pure N₂ flow with a temperature range of 303 to 423 K.

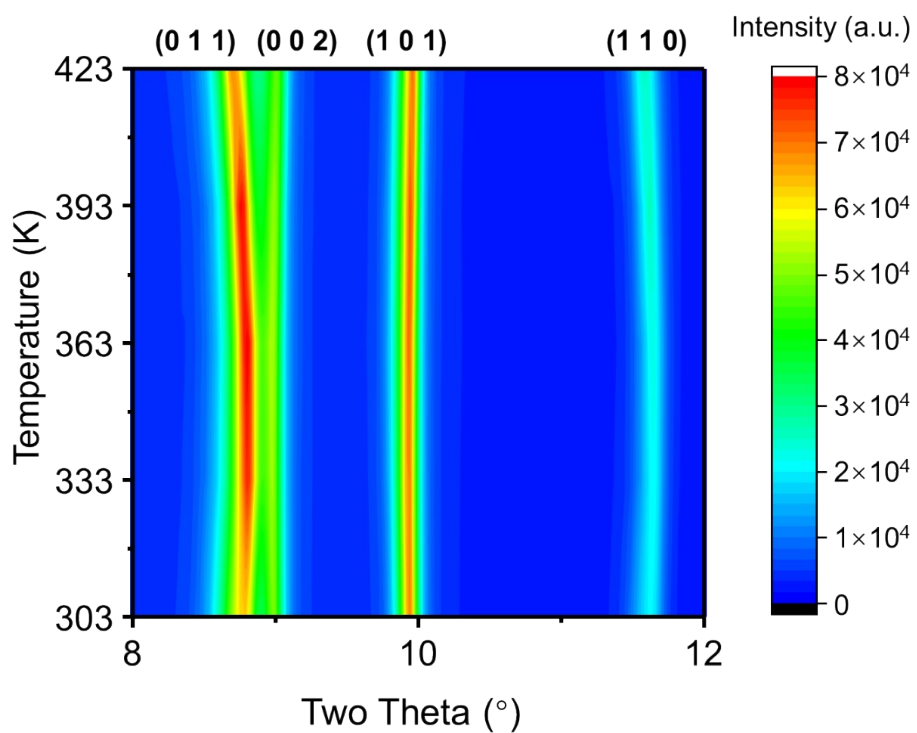


Figure S64. In-situ PXRD patterns of Hf-fum-FA under a 3-MP saturated N_2 flow with a temperature range of 303 to 423 K.

Table S1. Physical properties of hexane isomers.

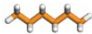

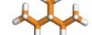

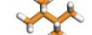
Hexane isomer	Structure	Kinetic diameter (Å)	Dimensional size (Å ³)	Boiling point (K)	RON
n-Hex		4.3	9.7 × 4.5 × 4.0	341.9	30
2-MP		5.0	9.2 × 6.4 × 5.3	333.4	74
3-MP		5.0	9.3 × 6.2 × 5.2	336.4	75
2,2-DMB		6.2	8.0 × 6.7 × 5.9	322.9	94
2,3-DMB		5.6	7.8 × 6.7 × 5.3	331.1	105

Table S2. Summary of Rietveld refinement.

Parameters	Zr-fum-FA	Zr-mes-FA	Hf-fum-FA
Crystal system	orthorhombic	orthorhombic	orthorhombic
Space group	<i>Immm</i>	<i>Immm</i>	<i>Immm</i>
<i>a</i> (Å)	10.02992(17)	10.0462(3)	9.97991(13)
<i>b</i> (Å)	12.1829(2)	12.3435(3)	12.11858(17)
<i>c</i> (Å)	19.7078(4)	19.6408(5)	19.6674(3)
$\alpha = \beta = \gamma$ (°)	90	90	90
Volume (Å ³)	2408.164	2435.565	2378.626
Calculated Density (g/cm ³)	1.785	1.831	2.541
R_{wp} (%)	5.19	6.27	4.42
R_p (%)	4.10	4.81	3.45
GoF (<i>S</i>)	1.6540	1.9982	1.5333
χ^2	2.7359	3.9929	2.3511

Table S3. Atom coordinates and occupancies of Zr-fum-FA.

Atom name	x	y	z	occupancy
O1	0.3668	0.38	0.1799	1
O2	0.2578	0.2842	0.1038	1
C1	0.2904	0.3036	0.1609	1
C2	0.2198	0.2498	0.2238	1
Zr1	0.5	0.5	0.12492	1
Zr2	0.32288	0.35249	0	1
O3	0.1077	0.3643	0	1
O4	0.3286	0.1704	0	1
O5	0.3289	0.5	0.0597	1
O6	0.5	0.6592	0.0612	1
C3	0	0.339	0.021	0.5

Table S4. Atom coordinates and occupancies of Zr-mes-FA.

Atom name	x	y	z	occupancy
O1	0.3751	0.3987	0.1862	1
O2	0.2545	0.2968	0.1042	1
C1	0.3039	0.3255	0.1644	1
C2	0.2237	0.2527	0.2218	1
C3	0.10987	0.18569	0.19043	0.5
Zr1	0.5	0.5	0.12612	1
Zr2	0.32191	0.35694	0	1
O3	0.1157	0.3655	0	1
O4	0.3373	0.1738	0	1
O5	0.3007	0.5	0.0664	1
O6	0.5	0.6482	0.0613	1
C4	0	0.339	-0.005	0.5

Table S5. Atom coordinates and occupancies of Hf-fum-FA.

Atom name	x	y	z	occupancy
O1	0.3613	0.3779	0.1773	1
O2	0.2619	0.2726	0.0866	1
C1	0.2773	0.3057	0.1436	1
C2	0.2253	0.2534	0.2224	1
Hf1	0.5	0.5	0.12432	1
Hf2	0.32324	0.35356	0	1
O3	0.10763	0.36282	0	1
O4	0.3373	0.1674	0	1
O5	0.3354	0.5	0.0528	1
O6	0.5	0.6536	0.0601	1
C3	0	0.36051	-1.05369	0.5

Table S6. Adsorption capacity of hexane isomers for various materials.

Material	Temperature (K)	Pressure (kPa)	Adsorption Capacity (mmol/cm ³)					Density (g/cm ³)	Ref.
			n-Hex	2-MP	3-MP	2,3-DMB	2,2-DMB		
Zeolite 5A	298	10	2.18	/	0.18	/	0.06	1.46	6,7
ZSM-5	298	10	2.24	/	0.43	/	0.09	1.81	7
Co-FA	298	10	2.11	/	2.17	/	0.15	1.87	7
Fe ₂ (BDP) ₃	403	10	1.60	1.47	1.53	1.52	1.51	1.15	8
Ca(H ₂ tcpb)	303	10	2.08	/	2.26	/	1.26	1.19	9
MIL-53-Fe-(CF ₃) ₂	313	10	0.44	/	0.41	/	0.33	1.56	10
Zr-abtc	298	10	3.20	/	1.62	/	0.78	1.20	7,11
Zr-bptc	423	6.67	1.84	/	0.20	0.05	/	1.52	11
ZIF-8	373	5	2.61	/	/	/	/	0.95	12
Zn ₂ (HBDC) ₂ (dmtrz) ₂	298	10	1.20	/	1.03	/	0.15	0.87	13
Zn(BDC)(Dabco) _{0.5}	313	10	0.28	/	0.03	/	0.02	0.83	14
CAU-10-H/Br	303	10	1.90	/	0.92	/	0.14	1.24	15
Al-bttotb	298	10	1.79	/	1.09	/	0.04	1.04	7,16
PTA	303	10	1.85	/	1.01	/	/	0.88	17
HIAM-302	298	10	1.81	/	1.01	/	0.13	1.15	18
Fe ₃ (μ ₃ -O)(6fdca) ₃	303	10	1.03	/	0.76	/	0.56	1.31	19
Zn-adtb	303	10	1.38	/	0.27	0.05	/	1.13	20

MIL-140B	343	10	0.76	0.51	0.44	0.18	0.14	1.55	21
MIL-160(Al)	423	10	1.50	1.34	1.13	0.87	0.65	1.10	22
Zn-tcpt	303	10	3.61	/	2.51	/	0.04	1.27	23
UU-200	303	10	2.57	1.90	1.71	0.55	0.13	1.58	24
NU-2002	298	1	1.57	1.66	1.60	1.52	1.03	1.17	25
NU-2200	298	10	1.68	1.34	1.16	0.23	0.17	1.34	26
MoOFOUR-Co-tpb	303	10	1.81	/	1.04	/	0.10	1.21	27
HIAM-203	303	10	2.49	/	2.20	/	0.07	1.62	28
HIAM-410LI	303	10	1.81	/	1.56	/	1.22	1.49	29
Ni-Asp	303	6.67	2.14	/	0.30	/	0.23	1.46	30
Mn-dhbq	303	6.67	2.78	/	2.77	1.24	/	1.56	31
Cu-CrO ₄ -TPA	303	10	1.32	0.89	0.80	0.19	0.08	0.94	32
NU-2004	298	10	1.39	0.82	0.84	0.27	0.26	1.09	33
Ni(4-PyC) ₂	303	10	2.08	/	1.12	0.17	/	1.22	34
CopzNi	303	10	2.89	1.95	/	/	0.11	1.33	35
HIAM-318	303	10	1.09	/	0.91	/	0.09	0.81	36
Zr-fum-FA	303	10	2.00	0.42	0.58	0.11	0.07	1.79	
	423	10	1.15	0.55	0.88	0.24	0.11		This work
Zr-mes-FA	303	10	1.41	0.33	0.35	0.06	0.06	1.83	
Hf-fum-FA	303	10	2.40	0.72	0.59	0.09	0.07	2.54	

Table S7. Heats of adsorption of hexane isomers on Zr-fum-FA, Zr-mes-FA, and Hf-fum-FA.

Material	Heats of Adsorption (kJ/mol)		
	n-Hex	3-MP	2-MP
Zr-fum-FA (DSC Run1)	38.5	25.6	12.7
Zr-fum-FA (DSC Run2)	40.2	22.4	19.3
Zr-fum-FA (DSC Run3)	38.8	20.7	15.6
Zr-fum-FA (DSC Average)	39.2 ± 0.9	22.9 ± 2.5	15.9 ± 3.3
Zr-fum-FA (Clausius-Clapeyron)	40.9	28.8	27.3
Zr-mes-FA (Clausius-Clapeyron)	53.9	36.6	36.1
Hf-fum-FA (Clausius-Clapeyron)	37.2	27.5	25.9

Table S8. The LDF mass-transfer coefficients of n-Hex on Zr-fum-FA, Zr-mes-FA, and Hf-fum-FA at varied temperatures.

Temperature (K)	Mass-Transfer Coefficients, $k_s a_p$ (s^{-1})		
	Zr-fum-FA	Zr-mes-FA	Hf-fum-FA
303	6.6117E-5	6.0430E-5	6.1527E-5
333	8.8168E-5	1.2864E-4	6.2643E-5
363	4.0679E-4	7.3653E-4	1.5400E-3
393	1.4600E-3	3.8500E-3	6.3800E-3
423	4.9600E-3	1.4590E-2	1.4860E-2

Table S9. Surface areas and pore volumes of as-synthesized Zr-fum-FA, Zr-mes-FA, and Hf-fum-FA, and corresponding samples after all hexane vapor adsorption-desorption tests.

Material	S_{BET} (m ² /g)	V_{total} at $p/p_0 = 0.95$ (cm ³ /g)
Zr-fum-FA fresh	440	0.185
Zr-fum-FA cycled	431	0.200
Zr-mes-FA fresh	351	0.138
Zr-mes-FA cycled	336	0.131
Hf-fum-FA fresh	348	0.140
Hf-fum-FA cycled	316	0.139

Table S10. DFT calculated energies of n-Hex on Zr-fum-FA at different diffusion coordinates.

Diffusion coordinate	Total energy of the system (eV)	
	Triangular pore	Rhombic pore
0	-52082.23678	-50191.96452
$a/12$	-52082.32860	-50191.98449
$a/6$	-52082.88686	-50191.98932
$a/4$	-52083.12720	-50191.99512

References

- 1 S. Wang, N. Xhaferaj, M. Wahiduzzaman, K. Oyekan, X. Li, K. Wei, B. Zheng, A. Tissot, J. Marrot, W. Shepard, C. Martineau-Corcoss, Y. Filinchuk, K. Tan, G. Maurin, C. Serre, *J. Am. Chem. Soc.*, 2019, **141**, 17207-17216.
- 2 E. Glueckauf, *Trans. Faraday Soc.*, 1955, **51**, 1540-1551.
- 3 S. J. Clark, M. D. Segall, C. J. Pickard, P. J. Hasnip, M. I. J. Probert, K. Refson, M. C. Payne, *Z. Kristall. Kristallogr. - Cryst. Mater.*, 2005, **220**, 567-570.
- 4 J. P. Perdew, K. Burke, M. Ernzerhof, *Phys. Rev. Lett.*, 1997, **77**, 3865-3868.
- 5 E. R. McNellis, J. Meyer, K. Reuter, *Phys. Rev. B*, 2009, **80**, 205414.
- 6 J. A. C. Silva, A. E. Rodrigues, *AIChE J.*, 1997, **43**, 2524-2534.
- 7 Q. Gong, L. Yu, J. Ding, S. Zhang, Y. Bo, K. Chi, H. Wang, Q. Xia, S. He, J. Li, *Sep. Purif. Technol.*, 2022, **294**, 121219.
- 8 Z. R. Herm, B. M. Wiers, J. A. Mason, J. M. van Baten, M. R. Hudson, P. Zajdel, C. M. Brown, N. Masciocchi, R. Krishna, J. R. Long, *Science*, 2013, **340**, 960-964.
- 9 H. Wang, X. Dong, E. Velasco, D. H. Olson, Y. Han, J. Li, *Energy Environ. Sci.*, 2018, **11**, 1226-1231.
- 10 P. A. P. Mendes, P. Horcajada, S. Rives, H. Ren, A. E. Rodrigues, T. Devic, E. Magnier, P. Trens, H. Jobic, J. Ollivier, G. Maurin, C. Serre, J. A. C. Silva, *Adv. Funct. Mater.*, 2014, **24**, 7666-7673.
- 11 H. Wang, X. Dong, J. Lin, S. J. Teat, S. Jensen, J. Cure, E. V. Alexandrov, Q. Xia, K. Tan, Q. Wang, D. H. Olson, D. M. Proserpio, Y. J. Chabal, T. Thonhauser, J. Sun, Y. Han, J. Li, *Nat. Commun.*, 2018, **9**, 1745.
- 12 A. Henrique, A. E. Rodrigues, J. A. C. Silva, *Sep. Purif. Technol.*, 2020, **238**, 116419.
- 13 Y. Ling, Z. X. Chen, F. P. Zhai, Y. M. Zhou, L. H. Weng, D. Y. Zhao, *Chem. Commun.*, 2011, **47**, 7197-7199.
- 14 P. S. B'arcia, F. Zapata, J. A. C. Silva, A. E. Rodrigues, B. J. Chen, *Phys. Chem. B*, 2007, **111**, 6101-6103.
- 15 Q. Yu, L. Guo, D. Lai, Z. Zhang, Q. Yang, Y. Yang, Q. Ren, Z. Bao, *Sep. Purif. Technol.*, 2021, **268**, 118646.

- 16 L. Yu, X. Dong, Q. Gong, S. R. Acharya, Y. Lin, H. Wang, Y. Han, T. Thonhauser, J. Li, *J. Am. Chem. Soc.*, 2020, **142**, 6925-6929.
- 17 Q. Chen, S. Xian, X. Dong, Y. Liu, H. Wang, D. H. Olson, L. J. Williams, Y. Han, X.-H. Bu, J. Li, *Angew. Chem. Int. Ed.*, 2021, **60**, 10593-10597; *Angew. Chem.*, 2021, **133**, 10687-10691.
- 18 L. Yu, S. Ullah, K. Zhou, Q. Xia, H. Wang, S. Tu, J. Huang, H.-L. Xia, X.-Y. Liu, T. Thonhauser, J. Li, *J. Am. Chem. Soc.*, 2022, **144**, 3766-3770.
- 19 D. Lv, H. Wang, Y. Chen, F. Xu, R. Shi, Z. Liu, X. Wang, S. J. Teat, Q. Xia, Z. Li, J. Li, *ACS Appl. Mater. Interfaces*, 2018, **10**, 6031-6038.
- 20 E. Velasco, S. Xian, H. Wang, S. Teat, D. Olson, K. Tan, S. Ullah, T. Popp, A. Bernstein, K. Oyekan, A. Nieuwkoop, T. Thonhauser, J. Li, *ACS Appl. Mater. Interfaces*, 2021, **13**, 51997-52005.
- 21 A. Henrique, T. Maity, H. Zhao, P. F. Brântuas, A. E. Rodrigues, F. Nouar, A. Ghoufi, G. Maurin, J. A. C. Silva, C. Serre, *J. Mater. Chem. A*, 2020, **8**, 17780-17789.
- 22 P. F. Brântuas, A. Henrique, M. Wahiduzzaman, A. von Wedelstedt, T. Maity, A. E. Rodrigues, F. Nouar, U.-H. Lee, K.-H. Cho, G. Maurin, J. A. C. Silva, C. Serre, *Adv. Sci.*, 2022, **9**, 2201494.
- 23 L. Yu, S. Ullah, H. Wang, Q. Xia, T. Thonhauser, J. Li, *Angew. Chem. Int. Ed.*, 2022, **61**, e202211359; *Angew. Chem.*, 2022, **134**, e202211359.
- 24 Z. Zhang, S. B. Peh, C. Kang, K. Yu, D. Zhao, *Angew. Chem. Int. Ed.*, 2022, **61**, e202211808; *Angew. Chem.*, 2022, **134**, e202211808.
- 25 C. S. Smoljan, Z. Li, H. Xie, C. J. Setter, K. B. Idrees, F. A. Son, F. Formalik, S. Shafaie, T. Islamoglu, L. K. Macreadie, R. Q. Snurr, O. K. Farha, *J. Am. Chem. Soc.*, 2023, **145**, 6434-6441.
- 26 B. Lal, K. B. Idrees, H. Xie, C. S. Smoljan, S. Shafaie, T. Islamoglu, O. K. Farha, *Angew. Chem. Int. Ed.*, 2023, **62**, e202219053; *Angew. Chem.*, 2023, **135**, e202219053.
- 27 Y. Su, R. Chen, P. Zhang, X. He, X. Liu, Y. Liu, H. Xiong, Z. Zhao, J. Luo, J. Chen, S. Chen, Z. Zeng, Z. Bao, S. Deng, J. Wang, *AIChE J.*, 2023, **69**, e17937.
- 28 Y. Lin, L. Yu, S. Ullah, X. Li, H. Wang, Q. Xia, T. Thonhauser, J. Li, *Angew. Chem. Int. Ed.*, 2022, **61**, e202214060; *Angew. Chem.*, 2022, **134**, e202214060.

- 29 F.-A. Guo, J. Wang, C. Chen, X. Dong, X. Li, H. Wang, P. Guo, Y. Han, J. Li, *Angew. Chem. Int. Ed.*, 2023, **62**, e202303527; *Angew. Chem.*, 2023, **135**, e202303527.
- 30 R. Chen, F. Zhou, B. Sheng, Z. Zhang, Q. Yang, Y. Yang, Q. Ren, Z. Bao, *ACS Sustainable Chem. Eng.*, 2022, **10**, 11330-11337.
- 31 R. Chen, L. Li, D. H. Olson, L. Guo, L. Chen, Q. Yang, Q. Xu, Z. Zhang, Q. Ren, J. Li, Z. Bao, *Small*, 2023, **19**, 2207367.
- 32 R. Chen, F. Zheng, J. Li, Y. Liu, F. Zhou, H. Sun, Q. Yang, Z. Zhang, Q. Ren, Z. Bao, *Small Struct.*, 2024, **5**, 2300302.
- 33 K. B. Idrees, K. O. Kirlikovali, C. Setter, H. Xie, H. Brand, B. Lal, F. Sha, C. S. Smoljan, X. Wang, T. Islamoglu, L. K. Macreadie, O. K. Farha, *J. Am. Chem. Soc.*, 2023, **145**, 23433-23441.
- 34 F. Xie, L. Yu, T. Jenkins, J. Shutak, K. Tan, T. Thonhauser, H. Wang, J. Li, *ACS Materials Lett.*, 2024, **6**, 43-48.
- 35 F. Zheng, L. Guo, R. Chen, F. Zhou, Z. Zhang, Q. Yang, Y. Yang, Q. Ren, Z. Bao, *Chem. Eng. J.*, 2023, **460**, 141743.
- 36 X. Zhou, L.-L. Ma, L. Yu, K. Zhou, K. Xiong, Y. Gai, J. Li, H. Wang, *ACS Materials Lett.*, 2024, **6**, 928-932.